UNIVERSITY OF THESSALY

SCHOOL OF ENGINEERING

DEPARTMENT OF MECHANICAL ENGINEERING

GAS-SURFACE INTERACTIONS BETWEEN MONATOMIC GASES AND GOLD SURFACES IN FOURIER FLOW VIA MOLECULAR DYNAMICS

by

STAVROS PANTOPOULOS

Submitted in partial fulfillment of the requirements for the degree of Diploma in Mechanical Engineering at the University of Thessaly

Volos,2024

UNIVERSITY OF THESSALY

SCHOOL OF ENGINEERING

DEPARTMENT OF MECHANICAL ENGINEERING

GAS-SURFACE INTERACTIONS BETWEEN MONATOMIC GASES AND GOLD SURFACES IN FOURIER FLOW VIA MOLECULAR DYNAMICS

by

STAVROS PANTOPOULOS

Submitted in partial fulfillment of the requirements for the degree of Diploma in Mechanical Engineering at the University of Thessaly

Volos,2024

Approved by the Committee on Final Examination:

Advisor	Prof. Dimitris Valougeorgis, Professor, Department of Mechanical Engineering, University of Thessaly
Member	Dr. Konstantinos Ritos, Assistant Professor, Department of Mechanical Engineering, University of Thessaly
Member	Dr. Chris Dritselis, Department of Mechanical Engineering, University of Thessaly

Ευχαριστίες

Αρχικά, θα ήθελα να ευχαριστήσω τον επιβλέποντα καθηγητή κ. Δημήτρη Βαλουγεώργη για την εξαιρετική συνεργασία, την λεπτομερή καθοδήγηση και την πολύτιμη βοήθεια τα τελευταία χρόνια. Ακόμη, θα ήθελα να ευχαριστήσω τον επίκουρο καθηγητή κ. Κωνσταντίνο Ρήτο και τον διδάκτορα Χρήστο Δριτσέλη για την σημαντική βοήθεια και την καθοδήγηση τους σε κομβικά κομμάτια της διπλωματικής. Επίσης, θα ήθελα να ευχαριστήσω τον καθηγητή κ. Βασίλη Μποντόζογλου, τον διδάκτορα Αθανάσιο Μπασδάνη και τον διδάκτορα Σεραφείμ Μισδανίτη για την συνεργασία μας και την τεχνική υποστήριξη που μου παρείχαν. Ευχαριστώ τον Ιωάννη-Σταύρο Παναγιωτόπουλο για την άψογη συνεργασία μας, καθ' όλη την διάρκεια της σχολής, και την ηθική υποστήριξη του.

Τέλος. οφείλω ένα τεράστιο ευχαριστώ στους γονείς μου και στα αδέλφια μου, για την αμέριστη αγάπη τους, την υποστήριξή και την βοήθεια τους όλα αυτά τα χρόνια , στους οποίους αφιερώνω αυτήν την εργασία.

Σταύρος Παντόπουλος

GAS-SURFACE INTERACTIONS BETWEEN MONATOMIC GASES AND GOLD SURFACES IN FOURIER FLOW VIA MOLECULAR DYNAMICS

Stavros Pantopoulos

Department of Mechanical Engineering, University of Thessaly

Supervisor: Prof. Dimitris Valougeorgis

Abstract

In recent decades, the study of rarefied gas flows and gas-surface interactions has gained significant attention due to its critical role in various technological applications such as micro-electro-mechanical systems and in the field of aerospace engineering. Despite considerable progress in this field, the understanding of accommodation coefficients, which play a crucial role in characterizing gas-surface interactions, remains incomplete. This diploma thesis investigates the interactions of the Fourier flow between Argon and Helium molecules with Gold walls using molecular dynamics simulations. The aim is to extend the knowledge of how pressure and surface temperatures impact the accommodation coefficients and the computational effort required. The gas-gas and gas-wall interactions are described by the Lennard-Jones potential with ab-initio computations, and an EAM potential is applied to the walls. The computed results were compared with previous experimental and theoretical values and showed a strong correlation. It was found that pressure and surface temperatures not only impact the numerical values of the energy and momentum accommodation coefficients, but also influence the velocity correlation shape and distribution profile. It should be noted that only pressure affected the required computational time.

Key words: MD simulation, accommodation coefficients, gas-surface interactions, rarefied gas flow

ΑΛΛΗΛΕΠΙΔΡΆΣΕΙΣ ΜΟΝΑΤΟΜΙΚΩΝ ΑΕΡΊΩΝ ΚΑΙ ΤΟΙΧΩΜΑΤΟΣ ΧΡΥΣΟΎ ΣΤΗ ΡΟΉ FOURIER ΜΕ ΜΟΡΙΑΚΉ ΔΥΝΑΜΙΚΉ

Σταύρος Παντόπουλος

Τμήμα Μηχανολόγων Μηχανικών, Πανεπιστήμιο Θεσσαλίας

Επιβλέπων Καθηγητής: Δημήτρης Βαλουγεώργης

Περίληψη

Τις τελευταίες δεκαετίες, η μελέτη των αραιοποιημένων ροών αερίων και των αλληλεπιδράσεων αερίου-επιφάνειας έχει παρουσιάσει μεγάλο ενδιαφέρον λόγω των σημαντικών ρόλων τους σε διάφορες τεχνολογικές εφαρμογές όπως τα μικρό-ηλεκτρομηχανικά συστήματα και τον τομέα της αεροδιαστημικής μηχανικής. Παρά τη σημαντική πρόοδο σε αυτόν τον τομέα, η κατανόησή των συντελεστών αλληλεπίδρασης, οι οποίοι έχουν σημαντικό ρόλο στον χαρακτηρισμό των αλληλεπιδράσεων αερίου-επιφάνειας, παραμένει ελλιπής. Η παρούσα διπλωματική εργασία διερευνά τις αλληλεπιδράσεις της ροής Fourier μεταξύ μορίων Αργού και Ηλίου με τοιχώματα χρυσού χρησιμοποιώντας προσομοιώσεις μοριακής δυναμικής. Στόχος είναι να διευρυνθούν οι γνώσεις πάνω στους τρόπους με τους οποίους η πίεση και οι επιφανειακές θερμοκρασίες επηρεάζουν τους συντελεστές αλληλεπίδρασης και τον υπολογιστικό χρόνο που απαιτείται. Οι αλληλεπιδράσεις αερίου-αερίου και αερίου-τοιχώματος περιγράφονται από το δυναμικό Lennard-Jones με υπολογισμούς ab-initio και στα τοιχώματα εφαρμόζεται ένα δυναμικό EAM. Τα υπολογιστικά αποτελέσματα συγκρίθηκαν με προηγούμενες πειραματικές και θεωρητικές τιμές και έδειξαν ισχυρή συσχέτιση. Διαπιστώθηκε ότι η πίεση και οι επιφανειακές θερμοκρασίες όχι μόνο επηρεάζουν τις αριθμητικές τιμές των συντελεστών αλληλεπίδρασης ενέργειας και ορμής, αλλά επηρεάζουν επίσης το σχήμα και το προφίλ κατανομής των συσχετίσεων ταχύτητας. Πρέπει να σημειωθεί ότι μόνο η πίεση επηρέασε τον απαιτούμενο υπολογιστικό χρόνο.

Λέξεις-κλειδιά: Προσομοίωση μοριακής δυναμικής, συντελεστές αλληλεπίδρασης, αλληλεπίδραση αερίου-επιφάνειας, αραιοποιημένη ροή αερίου

Contents

LIST OF TABLES

LIST OF FIGURES

Chapter 1: **INTRODUCTION AND LITERATURE REVIEW**

1.1 Introductory material

The development of micro-and nanotechnology has gained the attention of many researchers and engineers in the last few decades. One of the most promising areas of this technological revolution is Micro-Electro-Mechanical Systems (MEMS), where their small size, high performance, low power consumption, and low cost have made them an attractive choice for a variety of engineering applications [1]. However, most gaseous MEMS are not in the continuum region, and the Navier–Stokes equations fail to accurately describe gas behavior. For further research and development on MEMS, a deep understanding of rarefied gas dynamics is required [2]. To quantify the degree of gas rarefaction, the Knudsen number is applied, which is the ratio of the mean free path of the gas molecules over the characteristic length of the flow. Depending on the Knudsen number, gas flow can be divided into the following four regimes, [3]. For Kn < 0.001, the flow is in the continuum regime and the Navier-Stokes equations can be applied. For 0.001 < Kn < 0.1, the flow is in the slip regime and modified boundary conditions should be applied with the Navier-Stokes equations. For 0.1 < Kn < 10 , the flow is in the transition regime and for Kn > 10, the flow is in the free molecular regime. In the transition and free molecular regimes, the Navier-Stokes equations are not valid and kinetic theory should be applied.

Gaseous MEMS applications are, mostly, in the transitional regime, where gas–surface collisions are equally important as gas–gas collisions due to high degree of rarefaction and large surface area to volume ratio [4]. The goal of kinetic theory is to bridge the macroscopic level quantities with the interactions at the microscopic level. In kinetic theory, the most applied model for gas-gas collisions is the Boltzmann model, where the interactions between the particles are binary and elastic. To describe the gas-surface interactions, boundary conditions at kinetic level are needed. The most widely applied boundary condition is the Maxwell model, where a fraction α of the collided particles is scattered diffusively, while the remaining fraction $1-\alpha$ is scattered specularly. In the Maxwell model, α represents the accommodation coefficient, which characterizes the energy and/or momentum exchange between the particles and surfaces. The complete specular model represents an elastic collision between the gas molecules and the body surface. Meanwhile, the complete diffuse model indicates that the gas molecules leave the body surface in an equilibrium condition similar to the wall temperature. Other more general mesoscopic level models are also available and may be accordingly employed. In all cases however, the models are of phenomenological type and include one or more accommodation coefficients, which must be specified via experimental work.

On the contrary, although MD simulations are computationally expensive, they constitute an efficient and accurate method to calculate accommodation coefficients. This is achieved by modelling and tracking the motion of every particle and allowing the simulation of each collision

event [3]. Of course, the reliability and accuracy of MD simulation results depend highly on the potentials describing the intermolecular forces. An accurate method for extracting the potential parameters that describe the gas-gas and gas-surface intermolecular forces is through ab initio computations based on quantum mechanics. Also, as it well-known, MD simulations are restricted to microscopic-level systems.

1.2 Thesis objective and itinerary

The primary objective of this diploma thesis is to model the gas-surface interaction of various monatomic gases via MD, to compute the associated momentum and energy accommodation coefficients characterizing the interaction and also to investigate the impact of the pressure and temperature on the accommodation coefficients. This is accomplished by simulating typical Fourier flow systems involving the monatomic gases of argon and helium particles, placed between two parallel gold walls. Emphasis is placed on the shapes and distribution profiles of the incoming and outcoming particle velocity correlations. In addition, macroscopic quantities of practical importance, such as the gas velocity, temperature, etc., derived from the microscopic interactions are reported.

The structure of the diploma thesis is as follows: Chapter 2 provides an in-depth analysis of molecular dynamics, focusing on theory, techniques, main principles, and limitations. In Chapter 3, a detailed description of the LAMMPS code, an open-source classical molecular dynamics code, is provided, along with a brief explanation of its features and capabilities. Chapters 4 and 5 contain the work performed in the present thesis. More specifically, in Chapter 4, the investigated Fourier flow setup is formulated and the employed methods are described, while in Chapter 5, the results of the MD simulations are presented. The results section includes the deduced momentum and energy accommodation coefficients, the macroscopic quantities, the impact of pressure and temperature on the results and the computational effort required for the simulations. Finally, in Chapter 6, a brief summary of the thesis and the conclusions are presented, indicating possible future work in the field.

1.3 Brief literature review

In recent years, the field of Molecular Dynamics (MD) simulations has witnessed remarkable progress along with the evolution of rarefied gas engineering applications, which has led many researchers to focus on gas-surface interaction studies. The literature review is very extensive and therefore, in this paragraph, only some previous works in the field of gas-surface interaction, closely related to the present work, are cited.

In 2009, Sun et al. [4] studied gas-surface interactions by modeling Ar gas between two parallel smooth Pt walls at different temperatures while maintaining the wall distance constraint. The study demonstrated a strong correlation between the temperature of the walls and the temperature difference across the walls with the energy accommodation coefficient.

In 2010, Spijker et al. [5] studied the same system as above of Ar-Pt and Xe-Pt. The study showed that the energy and momentum accommodation coefficients have a strong correlation with the mass of the gas, Lennard-Jones potential function for gas-surface particles, and temperature of the walls. In addition, a new method for calculating the energy and momentum accommodation coefficients is proposed that does not require the average equilibrium velocity of the thermal wall.

In 2012, Prabha et al. [6] studied a similar system by mixing Ar–Xe between the Pt walls at different mole fractions. It was shown that the accommodation coefficients increased with an increase in the amount of heavier gas in the mixture due to the interactions being more diffusive.

In 2011, Sun et al. [7] studied the impact of rough nanochannels on accommodation coefficients. The increase in surface nano-roughness results in particles being trapped in the walls and in multiple gas-surface collisions, causing the tangential momentum and energy accommodation coefficient to increase and the normal momentum accommodation coefficient to decrease.

In 2014, Nedea et al. [8] investigated the gas-surface interactions of a dilute gas, which refers to a gas with a very small number density, and the surfaces of two parallel walls. The study showed that the accommodation coefficients increase when the mass ratio decreases, and the most reliable way to compute the accommodation coefficients is from the heat flux quantities.

In 2017, Sha et al. [2] studied the effect of different mixing rules on the accommodation coefficients. It was shown that the Fender-Halsey mixing rules had the highest accuracy with the experimental data under different conditions.

In 2020, Nedea et al. [9] studied a similar situation, including potential parameters based on ab initio computations, and compared the parallel wall approach with the molecular beam approach. It was shown that the ab initio computations are in close agreement with the experimental data and are the most reliable for calculating the accommodation coefficients. In addition, it was shown that for the Knudsen number in the transition regime ($Kn < 1$), the parallel-wall approach yielded better results than the molecular-beam approach.

In 2009, Cao et al. [10] studied various reviews on gas-surface interactions and concluded that accommodation coefficients rely on both microscopic properties, such as the mass of the particles and the potential function, as well as the macroscopic properties, such as the temperature, and velocity of the flow, including the Knudsen number.

Chapter 2: **DESCRIPTION OF THE MOLECULAR DYNAMICS METHODOLOGY**

2.1 Molecular dynamics

Molecular Dynamics (MD) simulation is a computational method that numerically integrates Newton's equations of motion for atoms and molecules based on approximations from established physics. When a system contains more than two bodies, no analytical solutions exist, leading to a state of chaotic motion [11]. The goal of MD simulation is not to provide an exact prediction of the evolution of a system from a precisely defined initial condition. Instead, the main interest is in statistical predictions, which aim to predict the mean behavior of a system initialized in a partially known state [12]. This approach acknowledges the uncertainty of initial conditions and uses statistical methods to provide meaningful predictions. To work properly, MD simulation requires and provides information about the position and momentum of all atoms in each time step. In general, atoms are represented as point masses that interact through forces, depending on their distance [13].

The trajectory, velocity and acceleration of the atoms is calculated by Newton's law,

$$F = ma \tag{2.1}$$

where m is the mass of the atom, F is the sum of the forces applied to the atom, and α is the acceleration of the atom.

It should be noted that high accuracy is preserved in the calculations because they are based on a solid physical foundation [14], [15]. Intramolecular forces caused by bonds, angles, dihedrals, and impropers are assumed to not distort the rigid bodies. Therefore, in MD simulations, the forces within a rigid body can be ignored. MD simulations rely heavily on potential energy functions that have been strictly tested over time. This reliance often restricts the use of MD simulations to explore new materials due to the lack of suitable potential energy functions [15]. The accuracy of these potential energy functions is vital because they describe the dynamics of the system. Any inaccuracies can lead to incorrect descriptions of the dynamic behavior of the system. MD simulations are also important for studying gas-surface interactions (GSI), which, along with gas-gas interactions, determine gas dynamics in wall-bounded problems [3].

Despite the high cost and limitations of actual experiments, computer simulations have become a comparable alternative. MD simulations can be considered as virtual experiments. They provide a reliable method to examine the static and dynamic responses of a system under specific initial conditions. They allow for direct observation of a system's behavior through graphical user interfaces. Compared to real-world experiments, MD simulations can manage more complex problems, save time and resources, allow better management of vital intermediate processes, and

monitor system reactions on scales that are typically inaccessible in actual experiments [15]. Typical MD simulations are limited to systems containing $10^2 - 10^6$ atoms, within a simulation box of nanometer-scale size and a time frame of nanoseconds. Long MD simulations are mathematically constrained because of the accumulation of errors in the numerical integration of Newton's equations of motion [11], [14]. Despite these limitations, there is currently no alternative method that can address such a wide range of problems at the necessary level of detail, making MD methods vital for both pure and applied research. In MD simulation, to achieve an optimal result of the studied system and minimize statistical errors, the chosen time step should be as small as possible. A reliable method for choosing the optimal timestep is to set it as one-tenth of the smallest molecular vibration period of the system. Molecular vibration periods range between 1-10 fs. In most MD simulations, the time step is set to 1 fs [14], [15]. Keeping a small timestep guarantees that the system's particles do not go through drastic changes in their properties which results in maintaining the energy of the system and the forces acting on the particles. In addition, when harmonic springs or torsional interactions exist in the simulated system, a small timestep can keep up with the rapid internal changes in the particles [13].

The MD simulation procedure is outlined as follows [15].

Step 1: The initial atomic positions and velocities of the atoms, boundary conditions, and constraints are determined. The potential-energy function should also be specified in this step.

Step 2: The structural optimization and energy minimization of the initial structure are adjusted to be similar to an equilibrium structure based on the chosen potential energy function.

Step 3: The forces and equation of motion for each particle are calculated for a chosen time step Δt, based on the specified potential energy function.

Step 4: The positions and velocities of each particle are updated.

Step 5: Other physical quantities are calculated based on the position and velocity information calculated in step 4 [15].

2.2 Interaction computations

In MD simulations, three fundamental methods are used to compute the particle interactions. The all-pairs, cell-subdivision, and neighbor-list methods, where each option is used, depending on the simulated system as shown in Figure 1. In the upcoming studied setups, the neighbor-list method is applied.

The all-pairs method checks every pair of atoms and is the easiest method to apply. However, the efficiency of the method decreases significantly when the cutoff distance r_c is small compared

with the simulation region size. The all-pairs method is used only when the number of atoms Nm is very low, because the necessary computations can be as large as of order O(Nm^2) [13].

The cell subdivision method divides the simulation region into a grid, where the cell edge length is greater than the cutoff distance. By assigning atoms to every cell based on their positions, interactions between atoms can occur only if the atoms are in the same cell or in neighboring cells. If periodic boundaries are applied in the simulation region, to prevent an atom from interacting with its copy, the region size must be at least $4r_c$ so that the cell subdivision method can work properly [13]. By organizing the atoms using the cell subdivision method, the necessary computations are reduced to order of O(Nm).

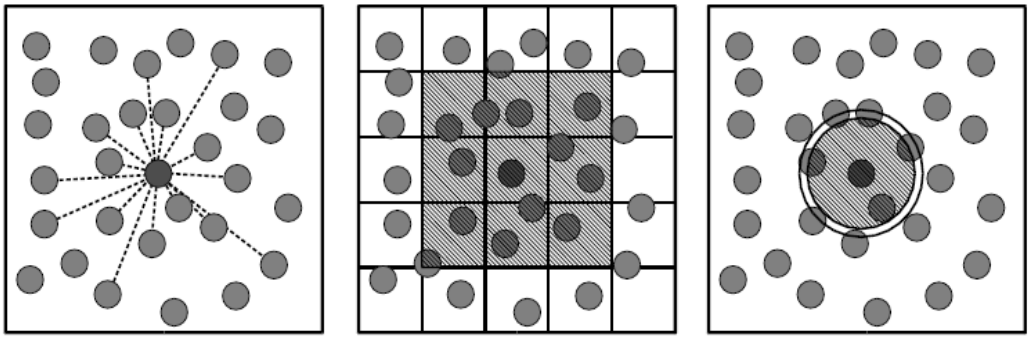

Figure 1: All pairs, cell subdivision (cell size exceed interaction distance) and neighbor-list (the circles show the interaction distance and chosen skin width).

Only 16% of the atoms inspected by the cell subdivision method are within the required interaction distance [13]. A more efficient method is the neighbor-list method, which creates a list for every atom in the simulation region and marks all its neighboring atoms that are inside the cutoff distance plus an extra distance called skin width (Δr) (shown in Figure 2) given by [14].

$$r_n = r_c + \Delta r \tag{2.2}$$

The main benefit of the neighbor-list method is the reuse of previous information to filter out atoms that are beyond the interaction distance. The frequency of refreshing the neighbor-list depends on checking the maximum velocity at every time step until:

$$\sum_{steps} \max\left(|v_i|\right) > \frac{\Delta r}{2\Delta t} \tag{2.3}$$

This restriction ensures that no atoms surpass the predefined distance r_n, which means that all interactions between atoms are listed. A typical update rate is 10-20 timesteps to ensure the highest simulation accuracy [15].

Using the neighbor-list method which only requires a local search to rebuild the neighbor-list every 10-20 timesteps, makes it the most efficient interaction computation method that critically reduces CPU time.

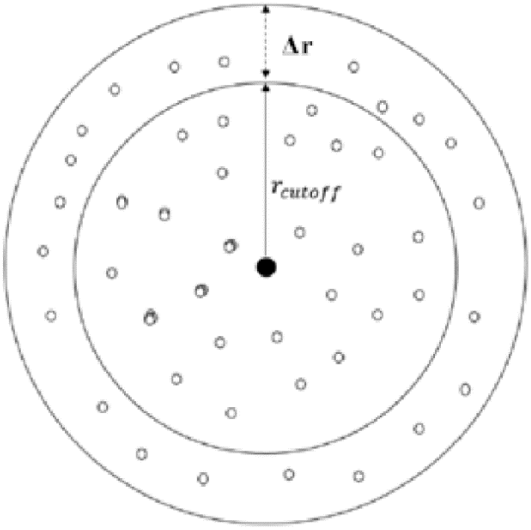

Figure 2: Illustration of the radial cutoff distance and the skin width of an atom (black dot).

2.3 Force fields and potential energy functions

2.3.1 Force fields

The most fundamental model to represent a substance in all three states (solid, liquid, and gas) is the use of spherical particles. Interactions between atoms can be simplified into two basic features: the interatomic force that is responsible for resisting compression, and the interatomic force that binds the atoms together in solid and liquid states. In general, force fields are constructed based on the Born-Oppenheimer approximation, which ignores electrons and assumes that the system energy depends only on the position of the nuclei [13], [15].

In MD simulations, force fields are calculated from the gradient of the potential energy function with respect to the position of the atoms. Choosing an appropriate potential energy function based on the phase of the working material is vital for obtaining reasonable results. A potential energy function created for a specific phase of a material does not necessarily apply to its other phases [15].

2.3.2 Lennard-Jones potential

The most well-known and applied two-body potential in MD simulations is the Lennard-Jones (LJ) potential, which is described by two parameters: ε and σ. Parameter ε refers to the strength of the interaction and σ refers to the closest distance between the two particles, where the potential energy is zero. The LJ potential can be calculated as [13].

$$V(r) = 4\varepsilon\left[\left(\frac{\sigma}{r}\right)^{12} - \left(\frac{\sigma}{r}\right)^{6}\right] \tag{2.4}$$

LJ potential has a highly repulsive core with a weakly attractive tail. Component $\left(\frac{\sigma}{r}\right)^{12}$ refers to the repulsive force that prevails at small distances, and $-\left(\frac{\sigma}{r}\right)^{6}$ refers to the attraction force that prevails over large distances. The cut-off distance r_c is defined as the distance where there is no interaction between atoms. Typically, in MD simulations, $r_c = 2.5\sigma$ [15].

For two different types of atoms, A and B, interacting with each other, the parameters σ_{AB} and ε_{AB} can be calculated by mixing rules. The most frequently mixing rule is the Lorentz-Berthelot model, where σ_{AB} and ε_{AB} are calculated as

$$\sigma_{AB} = \frac{1}{2}\left(\sigma_{AA} + \sigma_{BB}\right) \tag{2.5}$$

$$\varepsilon_{AB} = \sqrt{\varepsilon_{AA}\varepsilon_{BB}} \tag{2.6}$$

Instead of the arithmetic mean, the geometric mean can be used to calculate σ_{AB}:

$$\sigma_{AB} = \sqrt{\sigma_{AA}\sigma_{BB}} \tag{2.7}$$

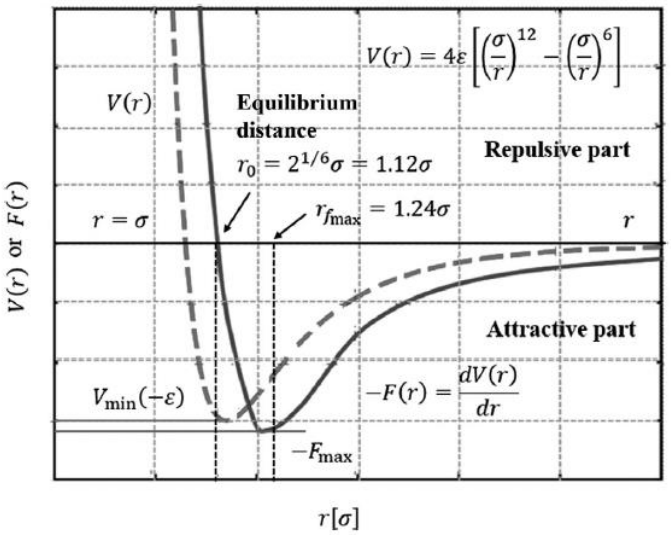

Figure 3: Lennard-Jones potential.

Another reliable method for calculating the interaction parameters of the LJ potential is ab initio computations, which provide high accuracy for computing the properties of the simulated system, such as energy and momentum accommodations. The Lennard-Jones simplified model has mutual characteristics with more complex models and has a huge advantage in terms of CPU time, but it is generally limited to gases at low density [13].

2.3.3 Embedded atom model potential

The embedded atom method (EAM) is explicitly used to simulate metallic bonds and provides information about the structure, vibrations, dynamics, phase transitions, diffusion, and separation [16], [17]. For the Lennard-Jones potential, the elastic constant ratio $C_{12}:C_{44}$ is equal to 1. Compared with FCC metals, the elastic constant ratio $C_{12}:C_{44}$ is between 2-4. High elastic constant ratios indicate the presence of many-atom interactions [17]. The pair potential fails to demonstrate the physics of metallic bonding because it ignores the many-atom interactions. The EAM potential is currently the most widely applied potential for simulating pure metals and alloys [15].

In the upcoming investigated setups, Lennard-Jones potential is applied to characterize the gas-gas and gas-wall interactions, while the embedded atom model potential is applied to characterize the wall-wall interactions.

2.4 Boundary conditions

The effect of particles that have fewer neighbors due to their location near the boundaries compared to the interior particles, causing the dynamics of the particles near the boundaries to differ from those of the interior particles, is called the surface effect. This effect can cause the simulation results to vary from reality and depend highly on the ratio of surface atoms to the total number of atoms in the system. In MD simulations, this ratio is proportional to $Nm^{-1/3}$ and will always be sufficiently large to affect the system. Thus, suitable boundary conditions such as periodic, fixed, or repulsive boundary conditions.[13], [15] must be applied.

A cell with atoms far from the surfaces is chosen and duplicated continuously in all three dimensions, creating an infinite simulation region of the primary cell copies. All atoms in the new simulation region have the same number of neighbors, resulting in the elimination of the surface effect. MD simulations require a constant number of atoms in the simulation region [13], [15].

Therefore, when periodic boundary conditions are applied and an atom exits from one side of the primary cell, a copy of the atom enters the primary cell from the other side as shown in Figure 4.

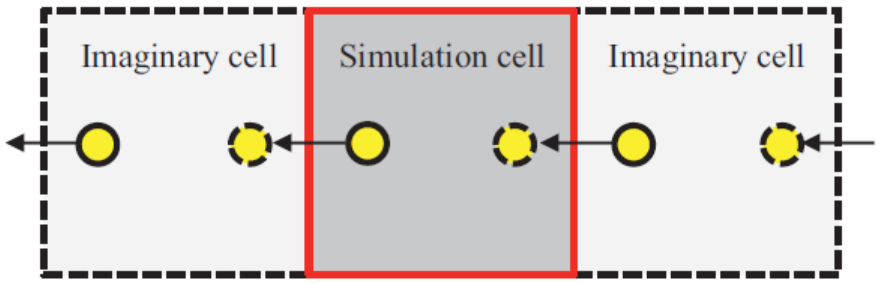

Figure 4: Simultaneous movement of the atom exiting and its copy entering the simulation cell.

Applying periodic boundary conditions results in an infinite number of image atoms, causing the number of interaction pairs to increase rapidly. To calculate these interactions, a minimum image criterion must be applied. The minimum image criterion is that atom *i* will interact with either atom *j* or an image of atom *j* based on which is closer as shown in Figure 5.

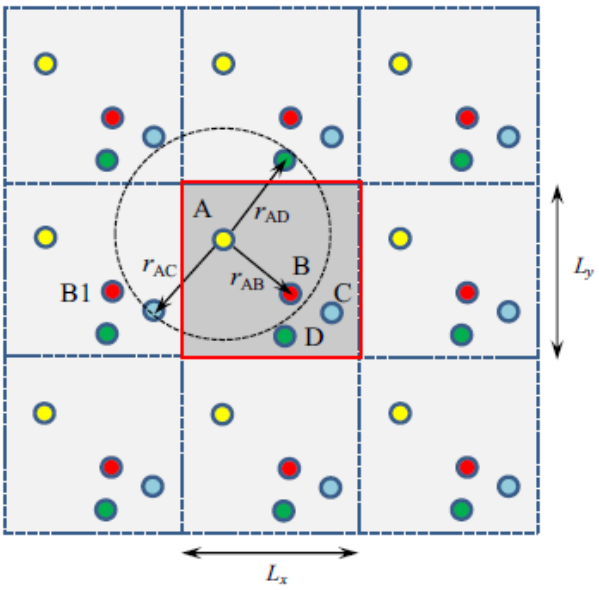

Figure 5: Atom A interacting with the closest neighbors based on minimum image criterion.

Under both repulsive and fixed boundary conditions, the energy of the system is kept constant. When repulsive boundary conditions are applied, the collision between the boundary and the particles is totally elastic, meaning that the velocity of the particle is reversed and the kinetic energy remains constant [15].

When fixed boundary conditions are applied instead of freezing the atoms as shown in Figure 6, resulting in unphysical dynamics, a spring potential is inserted into the particles, constraining them to vibrate only around their equilibrium state.

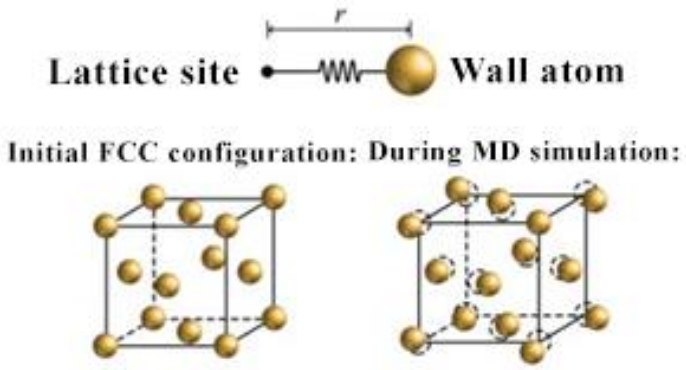

Figure 6: Illustration of fixed boundary condition.

2.5 Thermostats

In MD simulations, thermostats are classified into two categories. The first category is velocity-rescaling thermostats, which function by adjusting the velocities of particles to maintain the desired temperature. The second category is velocity-randomizing thermostats, which operate by randomizing particle velocities and ensuring a constant temperature distribution [15].

2.5.1 Simple velocity rescaling method

The simple velocity-rescaling method constitutes the first and most direct application of the thermostat model. Its working principle is based on the correlation between the average kinetic energy and temperature of the particles given by

$$\left\langle v^2 \right\rangle = \frac{k_B T}{m} \tag{2.8}$$

The velocities of the particles are modified by considering that they are proportional to the square root of the temperature as

$$v' = \sqrt{\frac{T}{T(t)}} v \tag{2.9}$$

where T(t) represents the temperature at each time step, and T is the desired temperature. It should be noted that the simple velocity-rescaling method does not allow temperature

fluctuations, leading to a non-physical behavior that cannot properly represent the dynamics of the system and the canonical ensemble.

2.5.2 Berendsen thermostat

To overcome this limitation, the Berendsen thermostat does not constrain the temperature, but uses exponential relaxation to the instantaneous temperature by applying a weakly coupled thermal bath.

Berendsen thermostat is rescaling the velocities of the particles by a factor ζ, that depends highly on the chosen timestep Δt, the difference between the instantaneous temperature T(t) and the desired temperature T and the coupling parameter τ_{T}. Factor ζ and the T(t) are given by

$$\zeta^2 = 1 + \frac{\Delta t}{\tau_{\mathrm{T}}}\left(\frac{T}{T(t)} - 1\right) \tag{2.10}$$

$$T(t) = T - C\exp\left(\frac{-t}{\tau_{\mathrm{T}}}\right) \tag{2.11}$$

The modified Newton equation of motion is expressed as

$$m_i \ddot{r}_i = -\frac{\partial U(R^N)}{\partial r_i} - \frac{1}{2\tau_{\mathrm{T}}}\left(\frac{\mathrm{T}}{\mathrm{T}(t)} - 1\right) m_i \dot{r}_i \tag{2.12}$$

The coupling parameter τ_{T} determines the frequency at which the particle velocities are rescaled.

The Berendsen thermostat is applied in the upcoming setups to control the walls temperature.

2.5.3 Stochastic couple method

The stochastic couple method applies a thermal bath to a system in which atoms collide with imaginary particles from the thermal bath at low probabilities, causing them to obtain random velocities that correlate with the desired temperature. The updated velocities are based on the Maxwell-Boltzmann distribution and are assigned to a selected group of atoms. Two well-known stochastic coupled thermostats are Andersen and Langevin. Due to its stochastic nature, the Andersen thermostat results in discontinuities in the dynamic properties of the system and it is only used to study structural properties. However, the Langevin thermostat implies the stochastic nature of the method to Newton's equation of motion with a factor that represents the interactions between smaller and larger atoms. This implementation allows the Langevin thermostat to accurately describe the dynamics of solute-solvent systems with high accuracy.

2.5.4 Nosé- Hoover thermostat

The fundamental idea behind the Nosé–Hoover thermostat is the use of an imaginary degree of freedom *s* that is implied in the potential energy function instead of the thermal bath seen in the previous thermostats. The Newton's equation of motion is modified as

$$m_i \ddot{r}_i = -\frac{\partial U(R^N)}{\partial r_i} - \gamma_i m_i \dot{r}_i \tag{2.13}$$

$$\frac{d\gamma_i(t)}{dt} = \frac{1}{Q}\left[\sum_{i=1} m_i \frac{v_i . v_i}{2} - \frac{3N+1}{2} k_b T\right] \tag{2.14}$$

Here, Q represents the imaginary mass of the extra degree of freedom s. The coupling strength of the thermostat is defined by the imaginary mass Q. However, in MD simulations, instead of using Q, a damping parameter τ_T is established, which controls the frequency with which the system temperature is relaxed. It should be noted that for certain systems, the Nosé–Hoover thermostat cannot reproduce the canonical ensemble.

Basconi [19], after simulating different types of thermostats, suggests that thermostats based on the velocity scaling method are most suitable to systems that need constant temperature and realistic dynamics, as shown in Figure 7. The velocity-scaling method thermostats provide highly accurate results in properties that occur in very short periods of time. In addition, it is shown that velocity scaling methods do not affect the kinetic properties.

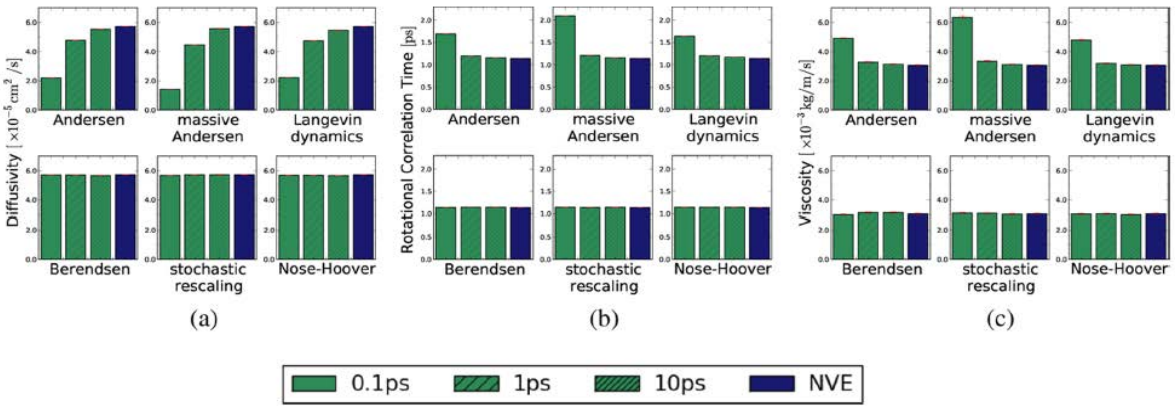

Figure 7: Different types of temperature control and coupling parameters.

2.6 Initial state and energy minimization

In MD simulations, the initial velocities of the particles are based on their initial temperature and can be calculated using the root square speed formula.

$$V_{RMS} = \sqrt{\frac{3RT}{MW}} \tag{2.15}$$

In addition, the center mass of the simulated system is set at rest. Every thermodynamic property is defined based on the average temperature $\langle T \rangle$ rather than the current temperature T at every time step. The aim of MD simulations is to study systems that have reached equilibrium to obtain reliable results. This implies that regardless of the initial configuration of the simulated system, it eventually reaches the equilibrium state [15]. A common method for setting the initial configuration is to uniformly distribute the particles in the simulation region. In 3D simulations, the typical lattices used are the FCC and simple cubic. In addition, it is recommended to remove any high-energy interactions by applying energy minimization [11]. Two methods are widely applied: the steepest descent method and the conjugate gradient method, both of which use the first-order derivative to achieve the lowest system energy. First-order derivative methods are applied to decrease the system energy and second-order derivative methods are applied to achieve the lowest energy value [15].

The main goal of energy minimization is to achieve the most stable atomic structure in terms of energy. It should be noted that an improperly applied initial configuration leads to longer times to reach thermal equilibrium. In the upcoming setups, the conjugate gradient method is applied to minimize the system energy.

2.7 Integration methods

In MD simulations, the most frequently applied integration methods are the Verlet method, leapfrog method and velocity Verlet method [13]. In the upcoming setups, the velocity Verlet method is applied.

2.7.1 Verlet method

The Verlet method applies a second-order Taylor series expansion to specify the position of each particle, given by.

$$x(t+\Delta t) = x(t) + v(t)\Delta t + a(t)\frac{\Delta t^2}{2} + \dot{a}(t)\frac{\Delta t^3}{6} + O(\Delta t^4) \tag{2.16}$$

$$x(t-\Delta t) = x(t) - v(t)\Delta t + a(t)\frac{\Delta t^2}{2} - \dot{a}(t)\frac{\Delta t^3}{6} + O(\Delta t^4) \tag{2.17}$$

By adding Eq. (2.16) and Eq. (2.17), the Verlet method position expression can be defined as

$$x(t+\Delta t) = 2x(t) - x(t-\Delta t) + a(t)\Delta t^2 + O(\Delta t^4) \tag{2.18}$$

By subtracting Eq. (2.17) from Eq. (2.16), the Verlet method velocity expression is defined as

$$v(t) = \frac{\left[x(t+\Delta t) - x(t-\Delta t)\right]}{2\Delta t} + O(\Delta t^2) \tag{2.19}$$

The main advantage of the Verlet method is that position and velocity calculations are time-reversible, and force-field calculations are required only once at every time step. Nevertheless, it should be noted that when Δt reaches extremely small values, it can cause a large error in the velocity expression due to the 1/Δt factor [15]. In addition, the position of the particles is independent of their velocity, which restricts the application of an external thermal bath in MD simulations.

2.7.2 Velocity Verlet method

The Velocity Verlet method is a modified version of the Verlet method. The main difference is that the position and velocity of the particles at t+Δt/2 are provided simultaneously from the information gathered at time t. The expressions that calculate the atomic position and velocity can be defined as

$$x(t+\Delta t) = x(t) + v(t)\Delta t + a(t)\frac{\Delta t^2}{2} + O(\Delta t^4) \tag{2.20}$$

$$v(t+\frac{\Delta t}{2}) = v(t) + \frac{\Delta t}{2}a(t) + O(\Delta t^2) \tag{2.21}$$

$$v(t+\Delta t) = v(t+\frac{\Delta t}{2}) + \frac{\Delta t}{2}a(t+\frac{\Delta t}{2}) + O(\Delta t^2) \tag{2.22}$$

The Velocity Verlet method significantly decreases errors in extended simulation runs compared to other integration methods based on particle acceleration [14]. In addition, the Velocity Verlet method conserves the energy and momentum of the system even if the time step is considerably small. In addition, the Velocity Verlet method is widely applied in MD simulations and, in general, in computational engineering [16].

2.7.3 Leapfrog method

Verlet modified the initial method by changing the velocity expression to avoid the errors created by the 1/Δt factor. The position expression can be modified as

$$x(t+\Delta t) = x(t) + \Delta t\left[v(t) + \frac{\Delta t}{2}a(t)\right] \tag{2.23}$$

$$v\left(t+\frac{\Delta t}{2}\right)=v(t)+\frac{\Delta t}{2}a(t) \tag{2.24}$$

$$v\left(t-\frac{\Delta t}{2}\right)=v(t)-\frac{\Delta t}{2}a(t) \tag{2.25}$$

Substituting Eq.(2.24) into Eq.(2.23) and subtracting Eq.(2.25) from Eq.(2.24), the position and velocity expressions of the leapfrog method are:

$$x(t+\Delta t)=x(t)+v\left(t+\frac{\Delta t}{2}\right)\Delta t+O(\Delta t^3) \tag{2.26}$$

$$v\left(t+\frac{\Delta t}{2}\right)=v\left(t-\frac{\Delta t}{2}\right)+a(t)\Delta t+O(\Delta t^3) \tag{2.27}$$

The leapfrog method, as shown in Figure 8, has an improved calculation accuracy, allowing an external thermal bath because the position of the particles depends on the velocity. It should be noted that the leapfrog method requires more storage, resulting in higher computing costs. In addition, it requires adaptations to specific simulated systems [13].

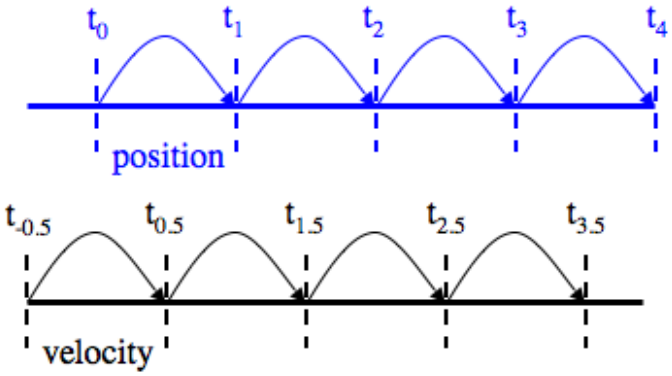

Figure 8: Leapfrog method.

2.8 Statistical ensembles, constraints and errors

An important factor in extracting reliable data on the average values of the properties is the use of a statistical ensemble that constrains the macroscopic conditions and leaves the microscopic details of the system unrestricted. The most commonly used statistical ensembles are the microcanonical (NVE), the canonical (NVT), the isothermal-isobaric (NPT), and the grand-canonical (μVT).

In the microcanonical ensemble, the number of particles N, volume of the system V, and the total energy E remain constant. It is applied to preserve statistical equilibrium in a closed system, where neither energy nor atoms can be exchanged with the environment.

In the canonical ensemble, the number of particles N, volume of the system V, and temperature T are constrained, and it is used to describe a closed system that can exchange thermal energy, but not particles, with the environment.

In the isothermal-isobaric ensemble, the number of particles N, pressure P, and temperature T remain constant. It is usually applied to systems that require a specific temperature and pressure to operate properly.

Finally in the grand-canonical ensemble, the chemical potential μ, volume V, and temperature T maintained constant. The system can exchange atoms and thermal energy with the environment. However, when applied, the computational cost increases rapidly due to the high number of degrees of freedom involved.

In most cases the isothermal-isobaric ensemble (NPT) is applied to decrease any initial stresses and the remaining simulation continuous with the microcanonical (NVE) ensemble. In addition, the canonical ensemble (NVT) is applied to manage the temperature of a specific region in the system, whereas the microcanonical ensemble is applied to the rest of the system [15].

In MD simulations, to maintain the simulated system under the desired operating conditions, three types of simulation constraints are used [15]. The first constraint refers to thermodynamic quantities that specify the macroscopic values of the system. These quantities are restricted to a group of three, which by default are the quantities of the microcanonical ensemble. The second constraint refers to the boundary conditions of the simulated region. The third constraint refers to the dimensions and geometry of the simulated region.

In MD simulations, there are three types of errors [13]:

- Regular errors depend on the numerical integration of the equations of motion, the interaction cutoff distance that is applied when the potential energy is close to zero, and the finite size of the simulation region, leading to errors in thermodynamic and structural properties. Regular errors are reproducible and an integral part of virtual experiments.
- Statistical errors depend on various fluctuations in the results.
- Insufficient data errors, where the system behavior cannot be expressed with high accuracy due to the lack of samples.

The quantum effect refers to a state in which classical dynamics cannot determine the properties of the system, and quantum mechanics calculations are required [15].

The uncertainty principle of Heisenberg indicates that the product of the uncertainty position and the uncertainty momentum is of the same order of magnitude as Planck's constant h [1], expressed as

$$|\Delta r|.|\Delta m| \sim O(h) \tag{2.28}$$

If the average momentum of a particle is much larger than Planck's constant, quantum effects can be ignored. The condition can be determined as

$$\left(3mkT\right)^{\frac{1}{2}} \gg n^{\frac{1}{3}}h \tag{2.29}$$

where n is the quantum number of rotations and vibrations , while $n^{-1/3}$ ~ mean molecular space.

In rarefied gas systems, the above condition is always satisfied because of the low density and high temperature, meaning that the properties of the system can be calculated from classical dynamics.

Chapter 3: **OPEN-SOURCE CODE "LAMMPS"**

3.1 Brief Description

The Large-scale Atomic/Molecular Massively Parallel Simulator code, with the abbreviation LAMMPS, is an open-source code simulating particles in all three states of matter, based on classical molecular dynamics [20] . It can simulate 2D and 3D systems with a large range of interatomic potential functions and boundary conditions to properly express the system behavior. The core code of LAMMPS constitutes only 10% of the total source code. The remaining 90% can be modified through commands and extensions, allowing the simulation of every possible system. Newton's equations of motion are integrated using the Velocity Verlet method, and the interaction computations are based on the neighbor-list method. LAMMPS provides the ability to observe crucial property values of the system, while the simulation is still running. LAMMPS can operate in both serial and parallel modes, where the serial mode is usually chosen for small systems and for debugging. The parallel mode is usually chosen for large complex systems to reduce the computational time. It should be noted that LAMMPS also has the ability to simulate systems in parallel mode by using both GPU and CPU, resulting in faster computations only on systems with non-hybrid potentials. Remarkably, LAMMPS offers the ability to extract important thermodynamic data for the system, atomic coordinates and velocities, and any per-atom or per-chunk kinetic and energy quantities. The features and capabilities of LAMMPS, from its flexible code structure to its efficient and reliable computational methods, have made it a widely used simulation tool in the scientific community.

3.2 Characteristics

LAMMPS includes a library of potential functions for computing pairwise interactions. LAMMPS provides the ability to set up hybrid model functions when atom types interact with different potential functions, for example, atom type *i* interacts with a LJ potential with atoms of the same type and with an EAM potential with atom type *j*. Table 1 presents various potential functions available in the LAMMPS library. Pair potential functions in LAMMPS can have multiple variations that are adapted to the specific requirements of different systems.

LAMMPS controls the temperature of the atoms using thermostats. The basic working principle of each thermostat is to calculate the current temperature of the system and attempt to modify it to the requested temperature. Table 2 lists the thermostats used in the LAMMPS library.

LAMMPS includes energy minimization algorithms so that the system can reach the most stable state with the lowest energy. The algorithms used in LAMMPS are listed in Table 3.

LAMMPS has the ability to define the boundary conditions in every dimension. The boundary conditions included in LAMMPS library are presented in Table 4.

An important factor in studying gas-surface interactions is understanding how walls interact with gas particles. These interactions can significantly affect the behavior of gas particles, particularly in confined systems. Table 5 includes some vital wall constraints in the LAMMPS library.

LAMMPS can provide output data in real time during the simulation and at the end of the simulation. This dual-mode output ability allows for continuous monitoring and post-processing analysis of the system. Table 6 includes the different output forms of LAMMPS library.

The highlighted values in Tables 1-5 are applied to characterize the upcoming setups.

Table 1: Indicative potential functions of LAMMPS library

Intermolecular Potentials	**Intramolecular Potentials**
Embedded atom	Harmonic bond
Lennard Jones	Morse bond
Buckingham	Multicentered Gaussian bond
Coulomb	Gromos

Table 2: Thermostats of LAMMPS library.

Nose-Hoover	Berendsen
Langevin	Direct rescaling

Table 3: Energy minimization algorithms of LAMMPS library

Conjugate gradient	Hessian-free truncated Newton
Steepest descent	Damped dynamics

Table 4: Boundary conditions of LAMMPS library.

Periodic	Non-periodic and fixed
Non-periodic and shrink-wrapped	Non-periodic and shrink-wrapped with a minimum value

Table 5: Wall constraints of LAMMPS library.

Set average force	Set specific force
Freeze particles	Move particles
Spring force	Reflective walls
Harmonic force	Granular walls

Table 6: Output forms of LAMMPS library.

Thermodynamic data	Per-atom quantities
Spatial and temporal values	Binary restart file

Chapter 4: **FOURIER FLOW CONFIGURATION**

The aim of the present work is to study the interactions between Argon (Ar) and Helium (He) molecules in Fourier flow with Gold (Au) walls. This will be achieved by computing the energy and momentum accommodation coefficients (E/MACs) and the macroscopic quantities for different cases. The effects of various number densities, as well as of wall temperatures are studied,

4.1 Formulation

The simulated system is a three-dimensional region where the monoatomic gas is surrounded by two parallel Au walls. Figure 9 shows a 2D XY cross-section schematic of the simulated region, where the red and blue atoms represent gold and gas particles, respectively.

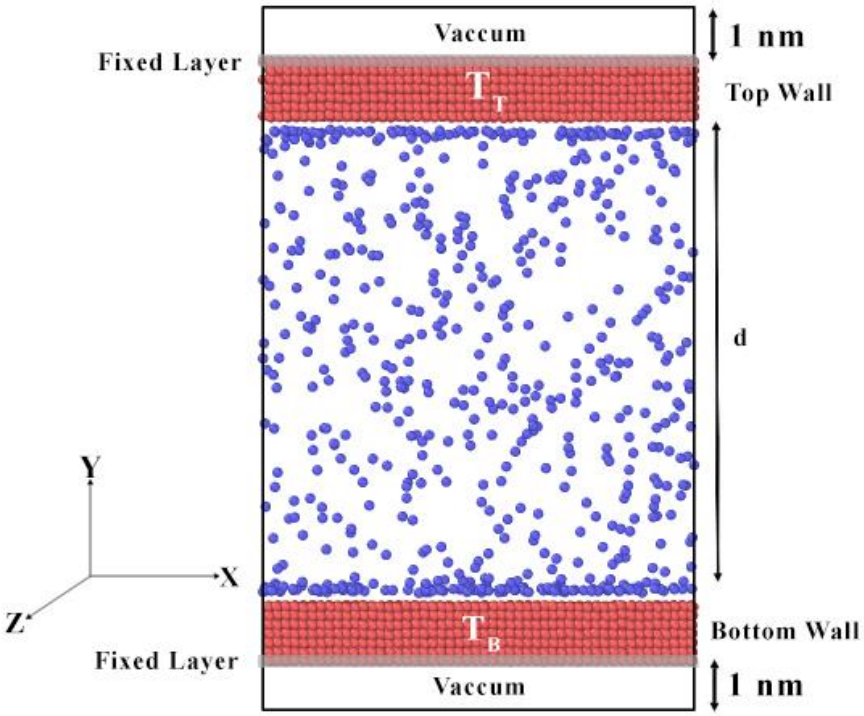

Figure 9: 2D simulated system schematic.

The cross-section of XZ is 10 × 10 nm. Each Au wall has a thickness of 1.25 nm and follows an FCC structure, consisting of 8750 particles.

The temperatures of the top wall T_T and the bottom wall T_B are controlled using Berendsen thermostats with a damping constant of 100 fs. Periodic boundary conditions are applied in all three dimensions. To avoid any rotational motion, a spring potential is applied to fix the furthest layer of the walls, which is shown as a gray layer in Figure 9. Two vacuum layers of 1 nm are placed outside the walls to avoid direct heat transfer between the walls. The initial temperature of the gas particles is uniformly set to 300K. After this, their temperatures only change through collisions. The distance between the walls for the various number densities scenario is set to d=11 nm for the Ar particles and d=102 nm for the He particles. In the various wall temperatures scenario, it is set to d=12 nm for the Ar particles and d=102 nm for the He particles. This is the closest distance that avoids surpassing the critical pressure in the system, which is 4.86 MPa and 0.23 MPa for Argon and Helium gases, respectively. The Au-Au interactions are expressed with an embedded atom model potential [21]. The gas-gas and gas-wall interactions are described by the Lennard-Jones potential. The well depth ε and zero potential distance σ, which are employed to calculate the Lennard Jones potential by applying Eq. (2.4), are based on ab-initio computations and are listed in Tables 7 and 8, including their molecular weights [22], [23]. Due to the utilization of ab-initio potential parameters, the application of mixing rules is not required.

Table 7: Potential parameters and molecular weights of Argon and Helium.

Atom Type	ε_{ii} [meV]	σ_{ii} [Å]	MW [a.m.u]
Au	229.4	2.63	196.96
Ar	12.2	3.35	39.94
He	0.94	2.64	4.00

Table 8: Potential parameters of Au-Ar and Au-He.

Parameter	Value
ε_{Au-Ar}	11.36 [meV]
σ_{Au-Ar}	3.819 [Å]
ε_{Au-He}	0.787 [meV]
σ_{Au-He}	4.342 [Å]

Table 9 presents the mathematical expressions used to calculate the various quantities of the simulated system. These expressions are vital for understanding the behavior and properties of the investigated systems. Table 10 provides the definitions of all variables used in the expressions listed in Table 9. The pressure expression is applied only for ideal gases, while the MD simulation pressure expression can be applied for all gases.

Table 9: Expressions for various quantities.

Quantity	Expression
Temperature	$\frac{1}{3k_B} m\overline{v^2}$
Number density	$\frac{N}{V_{gas}}$
Shear stress	$\frac{1}{2}\sum_{n=1}^{N}\left(r_{1a}F_{1b} + r_{2a}F_{2b}\right)$
Heat flux	$\frac{1}{V}\left[\sum_i e_i v_i + \frac{1}{2}\sum_{i<j}\left(F_{ij}.(v_i + v_j)r_{ij}\right)\right]$
MD simulation pressure	$\frac{Nk_BT}{V} + \frac{1}{3V}\sum_{i=1}^{N}\vec{r_i}.\vec{f}_i$
Pressure	$\eta k_B T$
Knudsen	$\frac{k_B T d}{4\pi\sqrt{2}r^2 P}$

Table 10: Definition of every variable applied in Table 9

k_B : Boltzmann constant	F : Interaction force
m : Atom mass	r : Atom position
$\bar{v}$: Average velocity	v: Atom velocity
N : Number of atoms	e: Atom energy
V : Region volume	T : Temperature
η : Number density	d : Normal distance
r : Atom radius	P : Pressure

Table 11: Characteristics of the investigated setups.

System	Number of atoms	Number Density [1/nm^3]	Top Wall Temperature [K]	Bottom Wall Temperature [K]	Initial Gas Temperature [K]	Reference Knudsen
Ar-Au	649	0.59	350	300	300	0.3
	297	0.27	350	300	300	0.65
	198	0.18	350	300	300	0.98
	99	0.09	350	300	300	1.96
	800	0.67	300	300	300	0.24
	800	0.67	500	300	300	0.24
He-Au	490	0.048	350	300	300	0.68
	296	0.029	350	300	300	1.14
	194	0.019	350	300	300	1.74
	92	0.009	350	300	300	3.68
	400	0.039	300	300	300	0.85
	400	0.039	500	300	300	0.85

The initial characteristics and properties of each case study are listed in Table 11. The reference Knudsen number and number density are calculated using the expressions listed in Table 9, while the number of atoms and temperatures are defined in the setup of the simulated system. The reference Knudsen number is based on the pressure given from the Boltzmann equation mentioned in Table 9. Argon and helium have been selected because of their monatomic nature, chemical inertness, and the differences in their molecular mass. In addition, most MEMS are coated with gold surfaces due to their thermal and oxidation properties. The chosen temperatures are typical in micro- and nanotechnology applications. Finally, the employment of various pressures is to check how the Knudsen number (or pressure) affects the system properties.

A complete collision between a gas particle and the wall is defined by the double-crossing of a virtual border as shown in Figure 10 with a dotted line, which is located at a distance r_c from the wall, where r_c is the cut-off distance [23]. This ensures that when the particle crosses the virtual border, is no longer affected by the wall. The velocity of the particles is recorded when they surpass the virtual border, before and after the collision. It is important to note that once equilibrium has been established the net particles flux at the virtual border is zero, i.e. the wall does not absorb or emit particles (particles are only reflected at the wall).

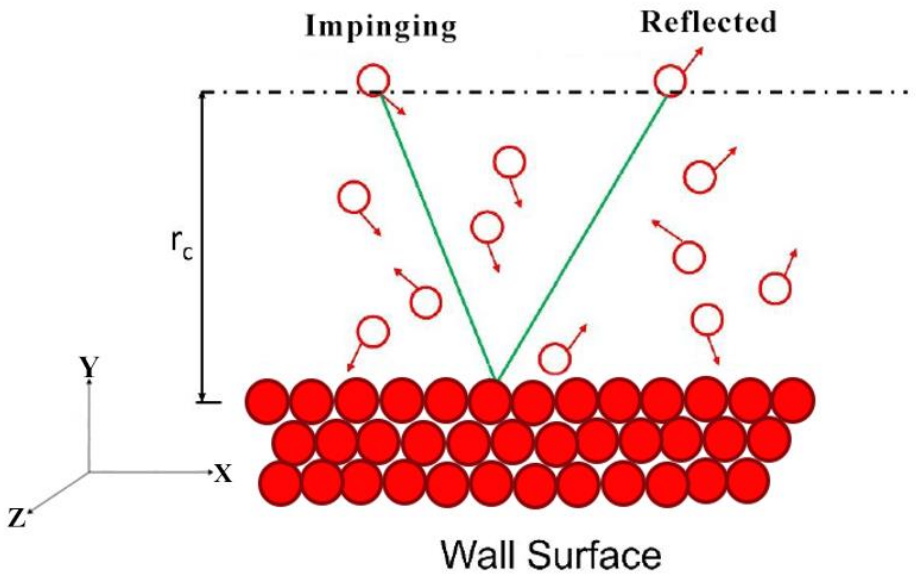

Figure 10: Virtual border schematic used to record the velocities of the collided particles.

4.2 Gas-surface interactions (GSI)

In rarefied gases, which are in the transition and free-molecular flow regimes (Kn>0.1), collisions between the gas molecules and the walls are dominant. Gas-surface interactions are responsible for the heat transfer and torque imposed by the wall on the gas molecules. Modeling and understanding gas-surface interactions are vital for studying rarefied gas systems and predicting their behavior under various conditions. Mathematical and phenomenological models at the mesoscopic scale, expressing gas-surface interactions, have in general low accuracy and more importantly require the knowledge of the involved accommodation coefficients. [3].

The most well-known and widely used method to study gas-surface interactions is the application of the Maxwellian boundary condition in system walls. The Maxwellian boundary condition states that the α fraction of the incoming molecules is scattered diffusely, while the remaining $1-\alpha$ fraction is scattered specularly.

The complete specular model represents an elastic collision between the gas molecules and the body surface [1].At the other end, the complete diffuse model indicates that the gas molecules leave the body surface in an equilibrium condition defined by the Maxwellian distribution according to the wall temperature. In most cases particles are scatted with some $0<\alpha<1$, i.e., combining diffuse and specular reflection. In general, it is expected that as the gas becomes heavier and the wall temperature reduces, the reflection becomes more diffuse. It should be noted that gas molecules do not reflect immediately from the surface but remain on the surface for a short time due to the interaction forces [18].

Knudsen defined an accommodation coefficient α to represent the percentage of gas molecules adjusted to the surface temperature according to

$$\alpha = \frac{\langle \kappa_I \rangle - \langle \kappa_O \rangle}{\langle \kappa_I \rangle - \langle \kappa_w \rangle} \tag{4.1}$$

Here, κ represents any kinematic or thermal quantity, such as momentum and energy of the particles, while the subscripts *I* and *O* stand for the associated incoming and outgoing quantities respectively, and subscript *w* stand for the fully diffuse reflection specified by the wall conditions [1]. The brackets indicate the average value of the chosen quantity. The main disadvantage of the Knudsen accommodation is that when $\langle \kappa_I \rangle$ is very close to $\langle \kappa_w \rangle$, numerical fluctuations are observed.

To overcome this limitation, Spijker [5] suggested a new method to calculate the accommodation based on a least-squares approximation, computing a first-order polynomial that expresses the collision data with high accuracy. The accommodation coefficient is calculated as $\alpha = 1 - c_1$, where c_1 is the slope of the first-order polynomial, which is obtained by the working data. The derivation of this supplementary relation is provided:

Consider some particle i with some incoming quantity $\kappa_{I,i}$ and the corresponding outgoing one $\kappa_{O,i}$, with $i - 1,...,n$. The objective is to find via the least square method the linear polynomial:

$$\kappa_O = c_0 + c_1 \kappa_I \tag{4.2}$$

The first step is to define the: $$d_i = \kappa_O - c_0 - c_1 \kappa_I \tag{4.3}$$

The goal is to minimize the value: $S = \sum_1^n \left(\kappa_O^i - c_0 - c_1 \kappa_I^i \right)$ (4.4)

$$\frac{dS}{dc_0} = 0 \rightarrow -2 \sum_1^n \left(\kappa_O^i - c_0 - c_1 \kappa_I^i \right) \tag{4.5}$$

$$\frac{dS}{dc_1} = 0 \rightarrow -2 \sum_1^n V_I^i \left(\kappa_O^i - c_0 - c_1 \kappa_I^i \right) \tag{4.6}$$

$$nc_0 = \sum_1^n \left(\kappa_O^i \right) - c_1 \sum_1^n \left(\kappa_I^i \right) \rightarrow c_0 = \frac{\sum_1^n \left(\kappa_O^i \right)}{n} - c_1 \frac{\sum_1^n \left(\kappa_I^i \right)}{n} \tag{4.7}$$

The constant : $c_0 = \langle \kappa_O \rangle - c_1 \langle \kappa_I \rangle$ (4.8)

To calculate the slope of the linear polynomial

$$\sum_{1}^{n} \kappa_I^i \left(\kappa_O^i - \langle \kappa_O \rangle + c_1 \langle \kappa_I \rangle - c_1 \kappa_I^i \right) = 0 \tag{4.9}$$

$$\sum_{1}^{n} \kappa_I^i \left(\kappa_O^i - \langle \kappa_O \rangle - c_1 \left(\kappa_I^i - \langle \kappa_I \rangle \right) \right) = 0 \tag{4.10}$$

$$\sum_{1}^{n} \kappa_I^i \left(\kappa_O^i - \langle \kappa_O \rangle \right) - \sum_{1}^{n} \kappa_I^i \left(c_1 \left(\kappa_I^i - \langle \kappa_I \rangle \right) \right) = 0 \tag{4.11}$$

The slope is expressed as follows: $c_1 = \dfrac{\sum_{1}^{n} \kappa_I^i \left(\kappa_O^i - \langle \kappa_O \rangle \right)}{\sum_{1}^{n} \kappa_I^i \left(\kappa_O^i - \langle \kappa_O \rangle \right)}$ (4.12)

Another way to express the slope coefficient more conveniently is by modifying the above equation.

$$\sum_{1}^{n} \kappa_I^i \left(\kappa_O^i - \langle \kappa_O \rangle \right) = \sum_{1}^{n} \kappa_I^i \left(\kappa_O^i - \langle \kappa_O \rangle \right) - \langle \kappa_I \rangle \sum_{1}^{n} \left(\kappa_O^i - \langle \kappa_O \rangle \right) \tag{4.13}$$

$$\rightarrow \sum_{1}^{n} \kappa_I^i \left(\kappa_O^i - \langle \kappa_O \rangle \right) - \sum_{1}^{n} \langle \kappa_I \rangle \left(\kappa_O^i - \langle \kappa_O \rangle \right) \tag{4.14}$$

$$\rightarrow \sum_{1}^{n} \left(\kappa_I^i - \langle \kappa_I \rangle \right) \left(\kappa_O^i - \langle \kappa_O \rangle \right) \tag{4.15}$$

Working the same way of the incoming velocity data

$$\sum_{1}^{n} \left(\kappa_I^i - \langle \kappa_I \rangle \right) \left(\kappa_I^i - \langle \kappa_I \rangle \right) \tag{4.16}$$

Therefore, the slope coefficient is: $c_1 = \dfrac{\sum_{1}^{n} \left(\kappa_I^i - \langle \kappa_I \rangle \right) \left(\kappa_O^i - \langle \kappa_O \rangle \right)}{\sum_{1}^{n} \left(\kappa_I^i - \langle \kappa_I \rangle \right) \left(\kappa_I^i - \langle \kappa_I \rangle \right)}$ (4.17)

The accommodation coefficient is expressed as: $\alpha = 1 - \dfrac{\sum_{1}^{n} \left(\kappa_I^i - \langle \kappa_I \rangle \right) \left(\kappa_O^i - \langle \kappa_O \rangle \right)}{\sum_{1}^{n} \left(\kappa_I^i - \langle \kappa_I \rangle \right) \left(\kappa_I^i - \langle \kappa_I \rangle \right)}$ (4.18)

When the accommodation coefficient is equal to zero, the collisions are completely specular, and when it is equal to one, the collisions are completely diffuse.

4.3 Summary of computed accommodation coefficients

The kinematic parameters employed to calculate the accommodation coefficients are the incoming and outcoming momentum and energy, which are obtained by estimating the corresponding velocities of the particles collided with the wall. Table 12 presents the incoming, outgoing, and thermal wall kinematic parameters, which are based on the velocity components of the particles, used to calculate each accommodation coefficient by applying Eq. (4.1) and Eq. (4.18).

Table 12: Specific kinematic parameters of each accommodation coefficient.

Accommodation coefficient/parameters	k_I	k_O	k_w [5]
Momentum of x-component α_x	Vx_I	Vx_O	0
Momentum of y-component α_y	Vy_I	Vy_O	$\frac{\sqrt{\pi}}{2}\sqrt{\frac{2k_BT}{m}}$
Momentum of z-component α_z	Vz_I	Vz_O	0
Tangential momentum TMAC	$\sqrt{Vx_I^2+Vz_I^2}$	$\sqrt{Vx_O^2+Vz_O^2}$	$\frac{\sqrt{\pi}}{2}\sqrt{\frac{2k_BT}{m}}$
Total momentum MAC	$\sqrt{Vx_I^2+Vy_I^2+Vz_I^2}$	$\sqrt{Vx_O^2+Vy_O^2+Vz_O^2}$	$\frac{3\sqrt{\pi}}{4}\sqrt{\frac{2k_BT}{m}}$
Energy of x-component α_{vx^2}	Vx_I^2	Vx_O^2	$\frac{k_BT}{m}$
Energy of y-component α_{vy^2}	Vy_I^2	Vy_O^2	$\frac{2k_BT}{m}$
Energy of z-component α_{vz^2}	Vz_I^2	Vz_O^2	$\frac{k_BT}{m}$
Total energy EAC	$Vx_I^2+Vy_I^2+Vz_I^2$	$Vx_O^2+Vy_O^2+Vz_O^2$	$\frac{4k_BT}{m}$
Tangential energy TEAC	$Vx_I^2+Vz_I^2$	$Vx_O^2+Vz_O^2$	$\frac{2k_BT}{m}$

4.4 Numerical Scheme

LAMMPS [20] is used to simulate all the flow setups discussed in this study. In the scenario related to various number densities, the timestep is $\Delta t = 1$ fs for both Ar and He, while in the scenario of various temperature differences, the timestep is $\Delta t = 1$ fs for Ar and $\Delta t = 0.5$ fs for He. In the former case, the equilibrium run time was set to 1 ns for the Ar-Au system and 3 ns for the He-Au system, while in the latter one, the equilibrium run time was set to 3ns for both systems. The running style applied is the velocity Verlet style. For the calculation of particle interactions, the neighbor-list method with binning and a skin distance of 2.5 Å is applied. The conjugate gradient method, on a 10^{-16} tolerance and 100.000 iterations, was applied for the energy minimization. To achieve statistically reliable results, the production simulation was ongoing until 100.000 collisions between gas particles and walls were completed [5], [24]. The virtual border shown in Figure 9 is located 12 Å from the wall for every case study of argon and helium.

The energy and momentum accommodation coefficients are calculated by Eq. (4.1) and Eq. (4.18) [5], using the recorded molecular velocity components of the gas particles. All computed energy and momentum accommodation coefficient calculated in this study will be compared with the corresponding results of similar studies [9], [25], that applied a different embedded atom model potential to the walls [26]. The flow diagram of equilibrium and production LAMMPS code are shown in Figure 11.

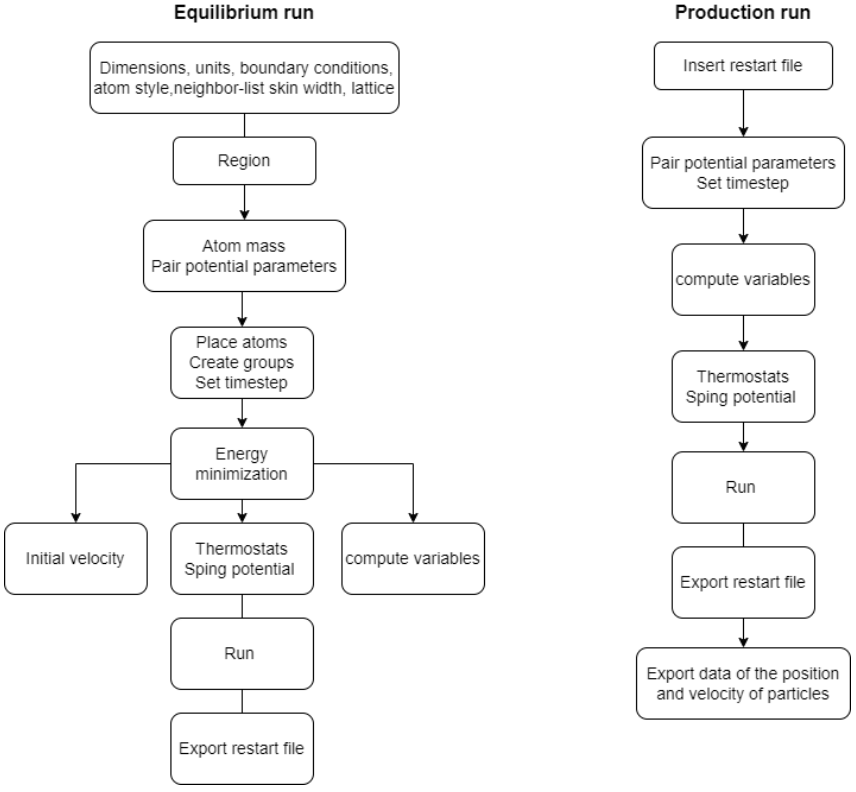

Figure 11: Flow diagram of equilibrium and production code.

Chapter 5: **RESULTS AND DISCUSSION**

5.1 Incoming and outcoming particle velocity components

After the MD simulations are completed, the data related to the three velocity components of the collided particles are processed to ensure that each data point was correlated to a collision. The incoming and outcoming velocity component correlations can be represented using 2D scatter plots. The linear polynomial expression, given by Eq. (4.2), is plotted using a red line. In addition, the slope of the red line (see Eq. (4.17)) is compared with the dashed horizontal and diagonal lines that represent the fully diffusive and specular models, respectively.

Correlations between the $x-$, $y-$ and $z-$components of momentum and the corresponding parts for energy of the Ar-Au and He-Au systems are shown in Figures 12–19, where the X- and Y-axes represent incoming and outgoing components, respectively. More specifically, Figures 12 and 13 refer to the Ar-Au setups, with number densities $\eta=\left[0.59,0.27,0.18,0.09\right]$, while Figures 14 and 15 refer to the He-Au setup, with number densities $\eta=\left[0.048,0.029,0.019,0.009\right]$. The bottom and top walls are set to $T=300K$ and $T=350K$, respectively. In Figure 12 the correlations are for the V_x, V_y and V_z components of the velocity and the associated momentum components and in Figure 13 the correlations are for $V_x^2+V_z^2$, V_y^2 and $V_x^2+V_y^2+V_z^2$ associated to the tangential, normal and total energies respectively, while in Figures 14 and 15 the corresponding correlations are provided for the He-Au setup. Figures 16 and 17 refer to the Ar-Au setups, while Figure 18 and 19 refer to the He-Au setup with surface temperatures of $T_B=300K/T_T=300K$ and $T_B=300K/T_T=500K$ for both setups. In Figure 16 the correlations are for the V_x, V_y and V_z components of the velocity and the associated momentum components and in Figure 17 the correlations are for $V_x^2+V_z^2$, V_y^2 and $V_x^2+V_y^2+V_z^2$ associated to the tangential, normal and total energies respectively, while in Figures 18 and 19 the corresponding correlations are provided for the He-Au setup.

The correlation shapes of the Ar-Au setups are wide because the collisions are highly diffusive while the correlation shapes of the He-Au setups are narrow because the collisions are highly specular. In addition, it is observed that V_x and V_z correlation shapes are almost similar in both Ar-Au and He-Au setups.

For the Ar-Au setups, with number densities $\eta=\left[0.59,0.27,0.18,0.09\right]$, the correlation shapes and the distribution profiles of $V_x, V_z, V_x^2+V_z^2$ and V^2 undergo minor changes in shape and size and become denser in the area around the specular model line, while V_y and V_y^2 exhibit the smallest changes, when the number density decreases.

For the He-Au setups, with number densities $\eta = [0.048, 0.029, 0.019, 0.009]$,the correlation shapes and the distribution profiles $V_x, V_z, V_x^2 + V_z^2$ and V^2 undergo minor changes in shape and size and become denser in the area around the specular model line while V_y and V_y^2 exhibit the smallest changes, when the number density decreases.

For the Ar-Au setups, with surface temperatures of $T_B = 300K / T_T = 300K$ and $T_B = 300K / T_T = 500K$, every correlation shape and distribution profile undergo minor changes, becoming denser in the area around the specular model line and larger in shape with increasing temperature.

For the He-Au setups, with surface temperatures of $T_B = 300K / T_T = 300K$ and $T_B = 300K / T_T = 500K$, every correlation shape and the distribution profile undergo minor changes, becoming denser in the area around the specular model line and larger in shape with increasing temperature.

5.2 Accommodation coefficients

In this study, α_x, α_y, α_z, α_x^2, α_y^2, α_z^2, MAC, TMAC, EAC, TEAC, that are shown analytically in Table 9, are calculated to obtain a full understanding of how the system parameters affect gas–surface interactions.

Momentum and energy accommodation coefficients of the Ar-Au and He-Au systems are shown in Tables 16-19. More specifically, Table 16 refers to the Ar-Au setups, with number densities $\eta = [0.59, 0.27, 0.18, 0.09]$, while Table 17 refers to the He-Au setup, with number densities $\eta = [0.048, 0.029, 0.019, 0.009]$. Table 18 presents the Ar-Au setups with surface temperatures of $T_B = 300K / T_T = 300K$ and $T_B = 300K / T_T = 500K$ while Table 19 presents the He-Au setups with surface temperatures of $T_B = 300K / T_T = 300K$ and $T_B = 300K / T_T = 500K$.

By comparing the energy and momentum accommodation coefficients of the Ar-Au and He-Au systems at varying pressures (number density), it was observed that a decrease in gas pressure correlates with a decrease in the energy and momentum accommodation coefficients, with the α_y exhibiting the smallest changes. As the gas pressure decreased, the gas collision behavior appeared to align more closely with that of the specular collision model.

By comparing the energy and momentum accommodation coefficients of the Ar-Au and He-Au systems at varying surface temperatures, it was observed that an increase in the surface temperature correlates with a decrease in the energy and momentum accommodation coefficients for the bottom wall at 300 K, while for the top wall at 500 K the energy and momentum

accommodation coefficients are increased compared with the bottom wall at 300 K on the He-Au system and a decrease on the Ar-Au system . As the temperature difference increased, the gas collision behavior appeared to align more closely with that of the specular collision model for the bottom wall at 300 K.

5.3 Macroscopic quantities

To understand the system behavior, the macroscopic quantities that emerged from the microscopic interactions are analyzed. A strong correlation between the experimental results and the theory of the Fourier flow will ensure the reliability of the results. A bin refers to a divided part of the simulated region, that is used to extract vital information on how a quantity evolves through the region.

From Figures 20-23 the temperature, normalized number density and bulk bin velocity for the Ar-Au and He-Au systems, respectively, where the X- and Y-axes represent the reference quantity and normal distance of the region, respectively. More specifically, Figures 20 and 22 refer to the Ar-Au setups, with number densities $\eta = [0.59, 0.27, 0.18, 0.09]$ and with surface temperatures of $T_B = 300K / T_T = 300K$ and $T_B = 300K / T_T = 500K$, respectively. Figures 21 and 23 refer to the He-Au setups, with number densities $\eta = [0.048, 0.029, 0.019, 0.009]$ and with surface temperatures of $T_B = 300K / T_T = 300K$ and $T_B = 300K / T_T = 500K$, respectively.

For the Ar-Au setups, it is shown that there is a linear relationship between the temperature and the normal distance in each case, except for the isothermal case, where the temperature is uniformly constant at 300 K. The behavior of the normalized number density distribution near the walls results from the attractive interaction potential of the walls [6], [27]. As the distance from the wall increases, there is no interaction effects and the normalized number density remains constant. The average bulk bin velocity in each case is near zero with small fluctuations.

For the He-Au setups, it is observed that both the temperature and normalized number density remain constant in the region in every case. This behavior can possibly be explained due to the highly specular collisions and the high thermal conductivity of helium. The average bulk bin velocity in each case is near zero with small fluctuations.

From Figures 24-27 the shear stresses of xy, xz, and yz for the Ar-Au and He-Au systems, respectively, where the X- and Y-axes represent the referred quantity and the normal distance of the region, respectively. More specifically, Figures 24 and 26 refer to the Ar-Au setups, with number densities $\eta = [0.59, 0.27, 0.18, 0.09]$ and with surface temperatures of $T_B = 300K / T_T = 300K$ and $T_B = 300K / T_T = 500K$, respectively. Figures 25 and 27 refer to the He-Au setups, with number densities $\eta = [0.048, 0.029, 0.019, 0.009]$ and with surface temperatures of $T_B = 300K / T_T = 300K$ and $T_B = 300K / T_T = 500K$, respectively.

For both Ar-Au and He-Au setups, it is shown that all three shear stresses have an average value near zero, with small fluctuations as it is expected from the theory of the Fourier flow.

From Figures 28-31 the heat flux in the x, y, and z directions for the Ar-Au and He-Au systems, respectively, where the X- and Y-axes represent the timestep and the referred quantity, respectively. More specifically, Figures 28 and 30 refer to the Ar-Au setups, with number densities $\eta = [0.59, 0.27, 0.18, 0.09]$ and with surface temperatures of $T_B = 300K / T_T = 300K$ and $T_B = 300K / T_T = 500K$, respectively. Figures 29 and 31 refer to the He-Au setups, with number densities $\eta = [0.048, 0.029, 0.019, 0.009]$ and with surface temperatures of $T_B = 300K / T_T = 300K$ and $T_B = 300K / T_T = 500K$, respectively.

For the Ar-Au setups, heat fluxes x and z have an average value of zero for all cases. The heat flux y has a negative average value because heat transfers from the top wall to the bottom wall, except in the isothermal case where the average value is zero. In the case of the non-isothermal state at $T_B = 300K / T_T = 500K$, it can be observed that the absolute average value is larger compared to the other cases because of the increased temperature difference.

For the He-Au setups , heat fluxes x and z have an average value of zero for all cases. Heat flux y has a negative average value because heat transfers from the top wall to the bottom wall, except in the isothermal case where the average value is zero. In the case of the non-isothermal state of $T_B = 300K / T_T = 500K$ it can be observed that the absolute average value is bigger compared to the other cases due to the increased temperature difference.

The strong correlation between the experimental data and theory ensures the reliability of the results.

5.4 Computational effort

Each MD simulation case was run on a university-provided computer, the specifications of which are listed in Table 13.

Table 13: Specifications of university provided computer.

CPU	Intel core i9-10900X 3.7GHz
GPU	NVIDIA GeForce RTX 2080 Ti 11GB
RAM	64 GB 2133MHz
SSD	Intel 660p Series M.2 2280 2TB

The MD simulation runs are executed using the MPI-GPU package of LAMMPS to minimize run time. Tables 14 and 15 show the required MD simulation time to record 100.000 collisions, run time, and some important simulation variables depending on the scenario. Run time increases as the number of atoms decreases because the rate of collisions decreases. The decrease in the number of atoms results in a decrease in the number density and pressure, while it increases the Knudsen number.

Table 14: Simulation variables and required simulation time of the Ar-Au and He-Au cases for various number densities.

System	Number Density ($1/nm^3$)	Number of atoms	Theoretical Pressure (MPa)	MD Pressure (MPa)	Kn	MD simulation time (ns)	Run time (hr)
Ar-Au	0.59	649	2.44	1.4	0.52	20	19
	0.27	297	1.12	0.6	1.22	50	46
	0.18	198	0.75	0.4	1.83	70	69
	0.09	99	0.37	0.2	3.66	100	94
He-Au	0.048	490	0.2	0.21	0.65	60	62
	0.029	296	0.12	0.13	1.06	90	94
	0.019	194	0.08	0.09	1.52	150	160
	0.009	92	0.04	0.04	3.43	250	255

Table 15: Simulation variables and required simulation time of the Ar-Au and He-Au cases for various temperature differences.

System	Bottom Wall Temperature (K)	Top Wall Temperature (K)	Number of atoms	MD Pressure (MPa)	Kn	MD simulation time (ns)	Run time (hr)
Ar-Au	300	300	800	1.2	0.56	25	38
	300	500	800	2.4	0.28	25	38
He-Au	300	300	400	0.16	0.86	100	155
	300	500	400	0.21	0.65	100	155

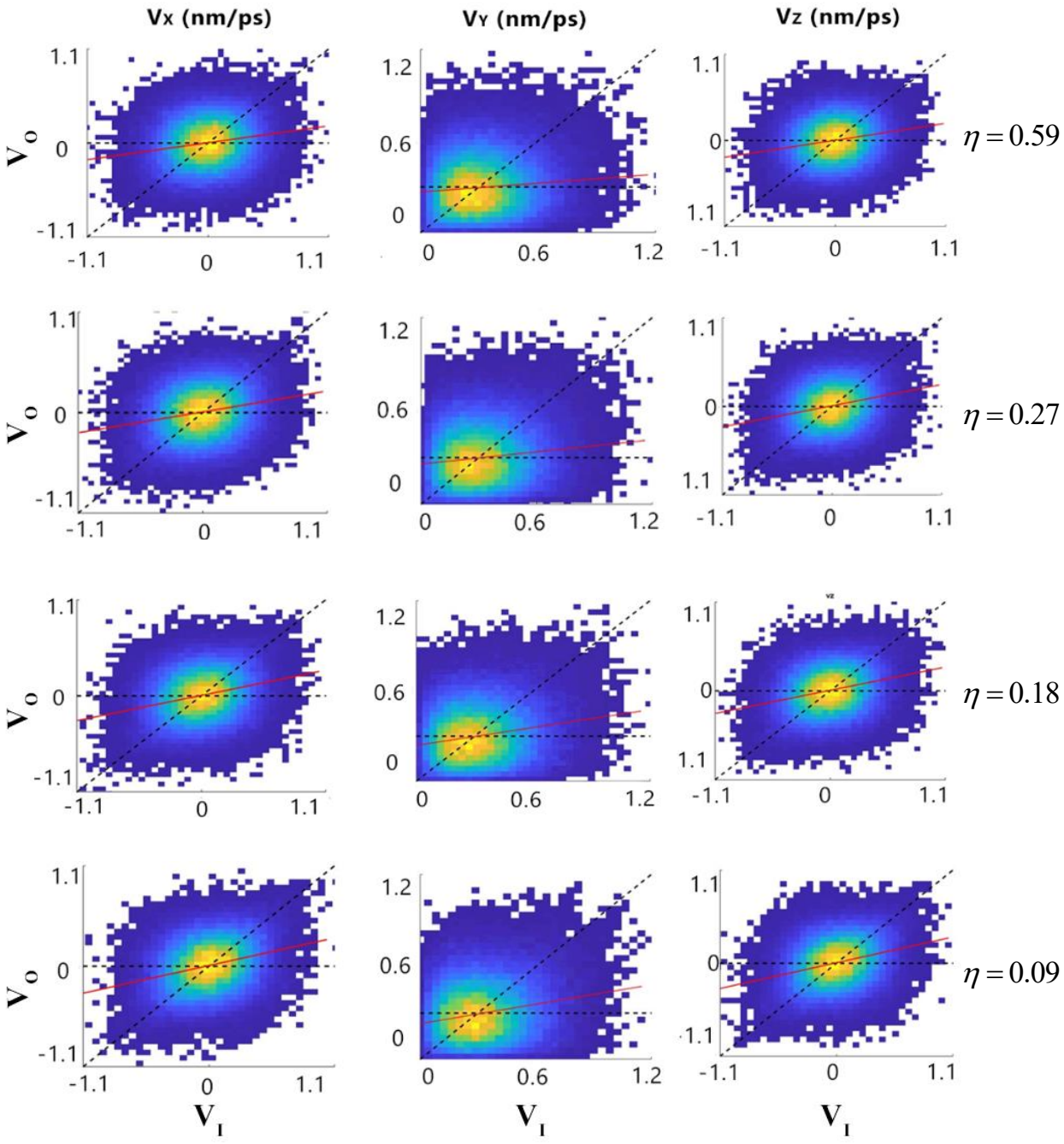

Figure 12: Velocity correlations of x-, y-, z- components of momentum of the Ar-Au system with number densities η=[0.59,0.27,0.18,0.09].

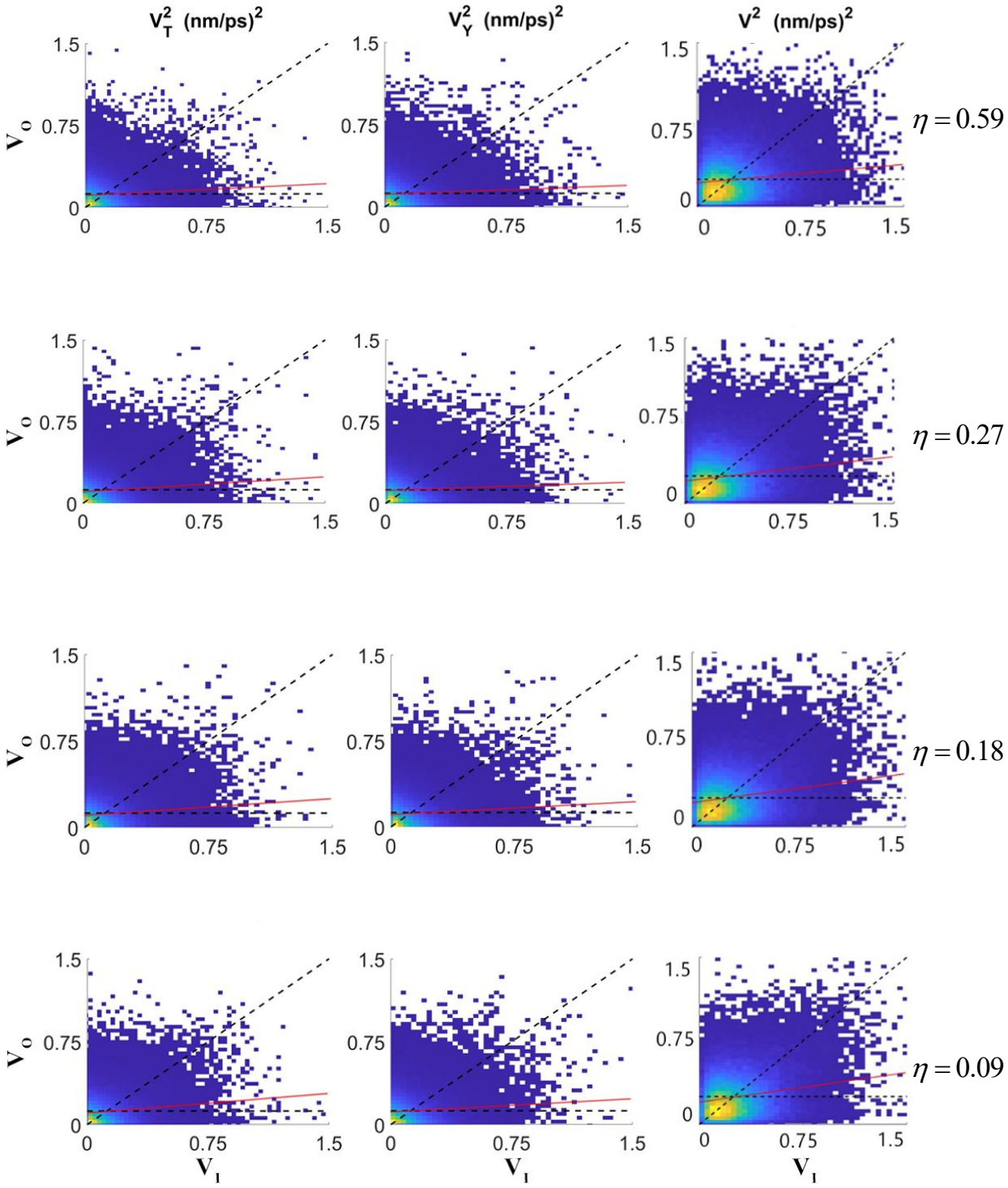

Figure 13: Energy correlations of the Ar-Au system with number densities η=[0.59,0.27,0.18,0.09].

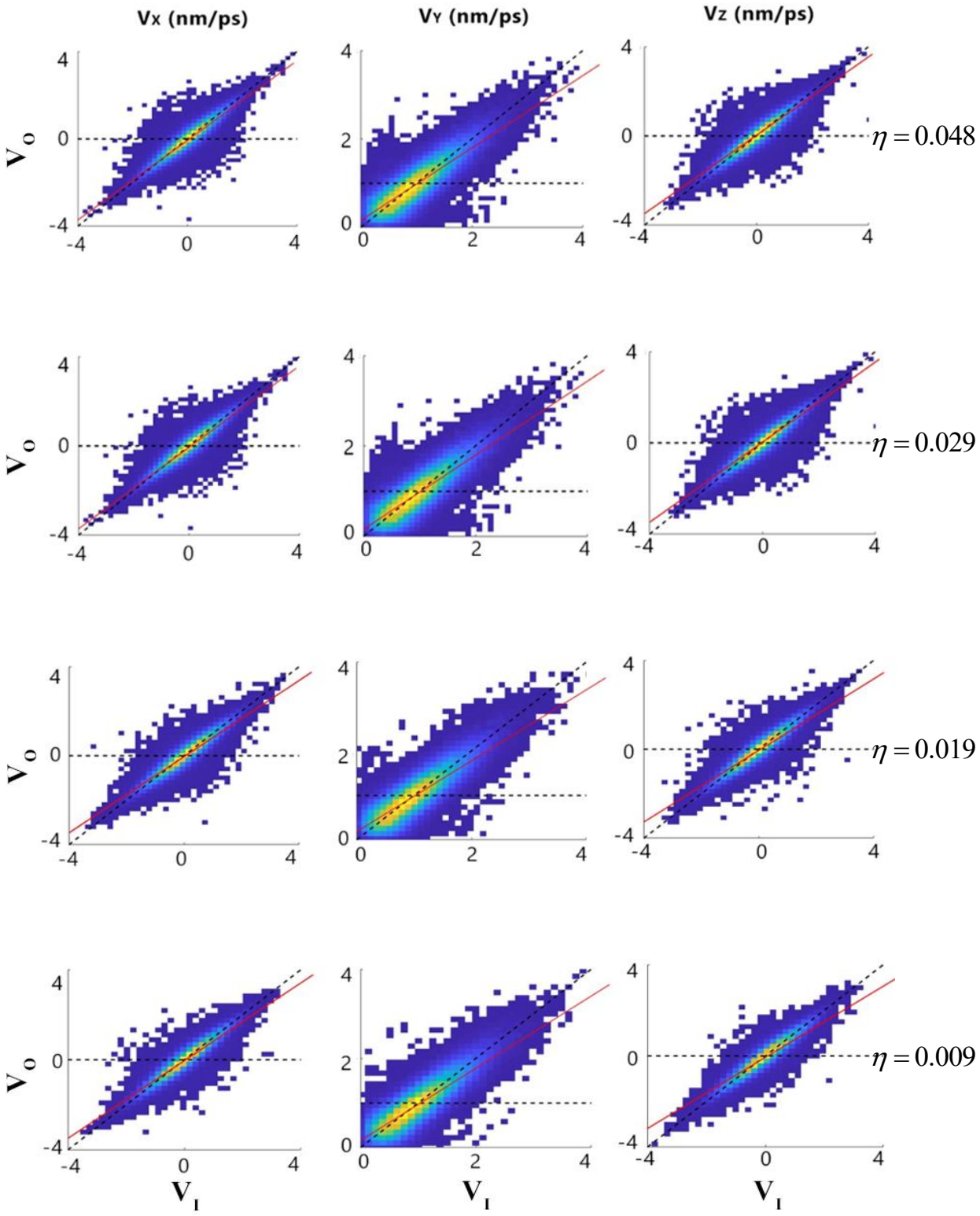

Figure 14: Velocity correlations of x-, y-, z- components of momentum of the He-Au system with number densities η=[0.048,0.029,0.019,0.009].

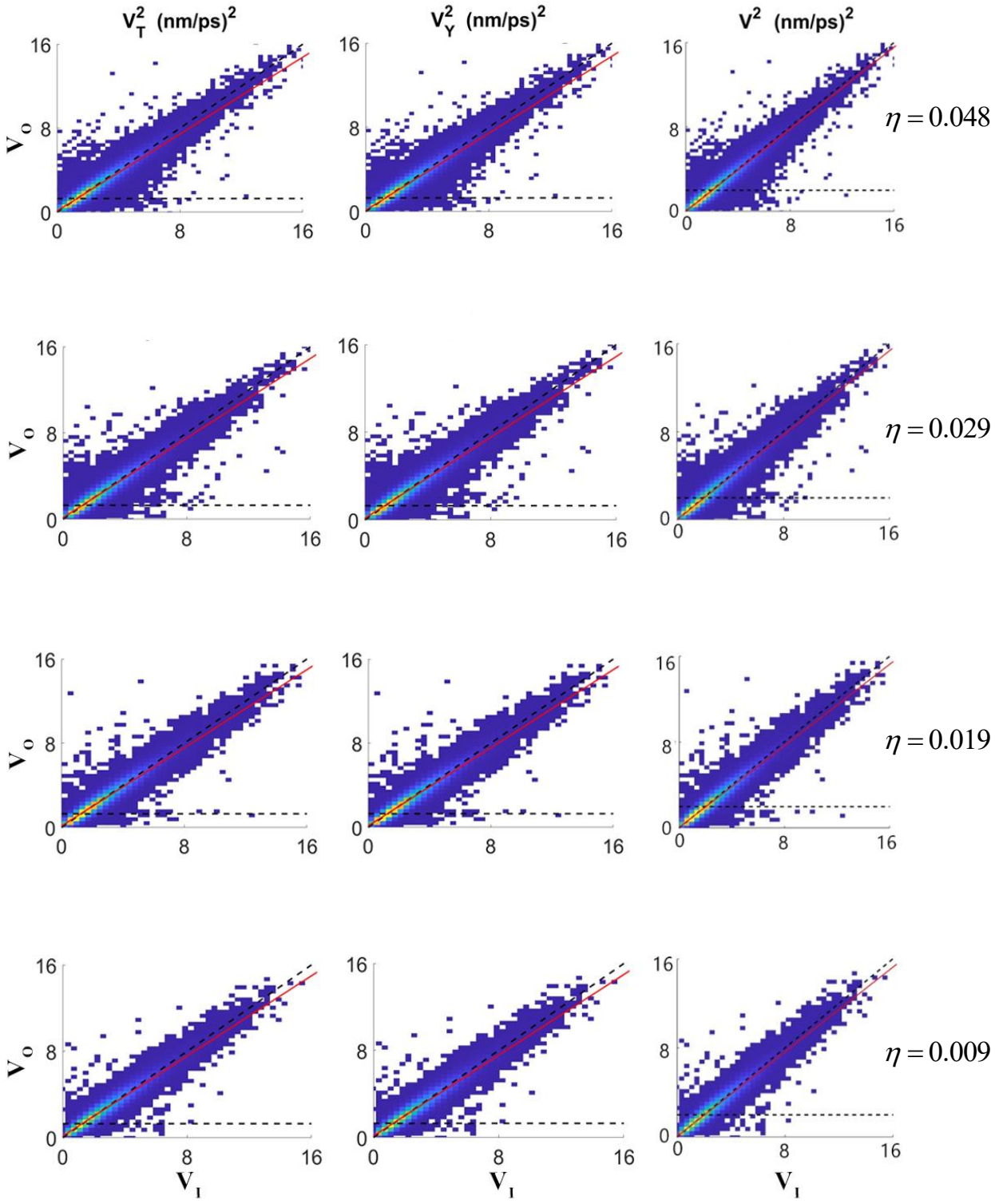

Figure 15: Energy correlations of the He-Au system at various number densities system with number densities η=[0.048,0.029,0.019,0.009].

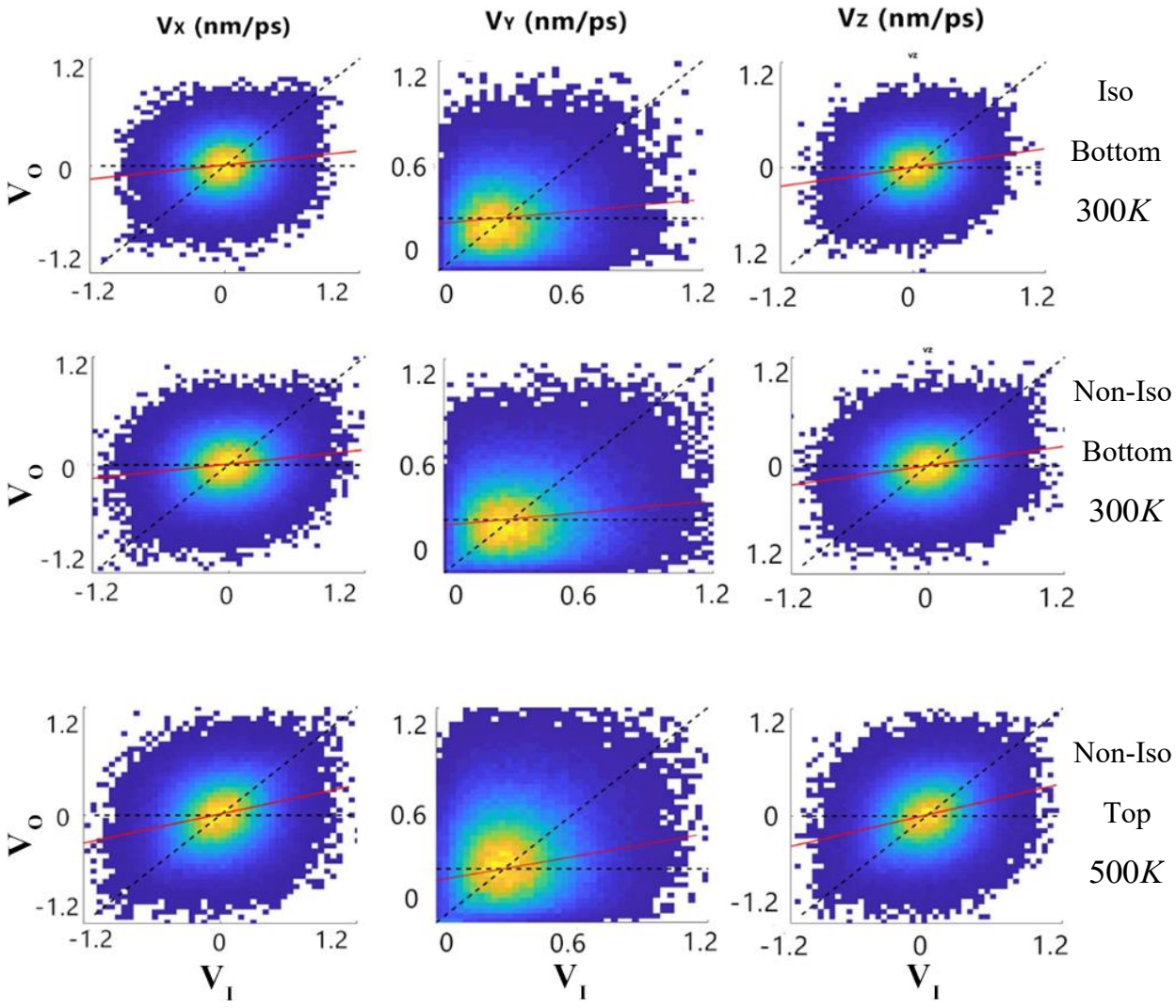

Figure 16: Velocity correlations of x-, y-, z- components of momentum of the Ar-Au system with surface temperature of T_B=300K/T_T=300K and T_B=300K/T_T=500K.

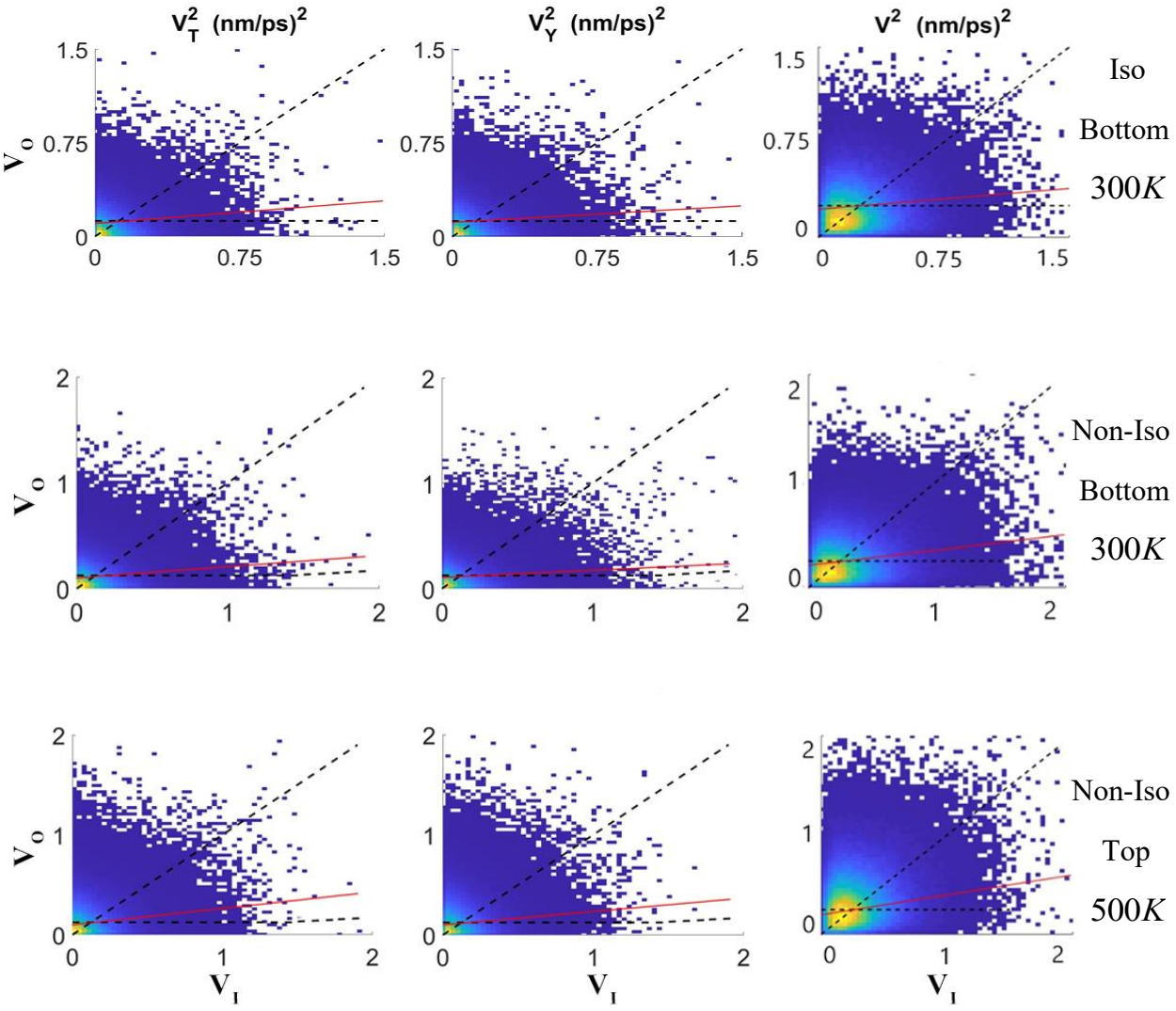

Figure 17: Energy correlations of the Ar-Au system with surface temperature of T_B=300K/T_T=300K and T_B=300K/T_T=500K.

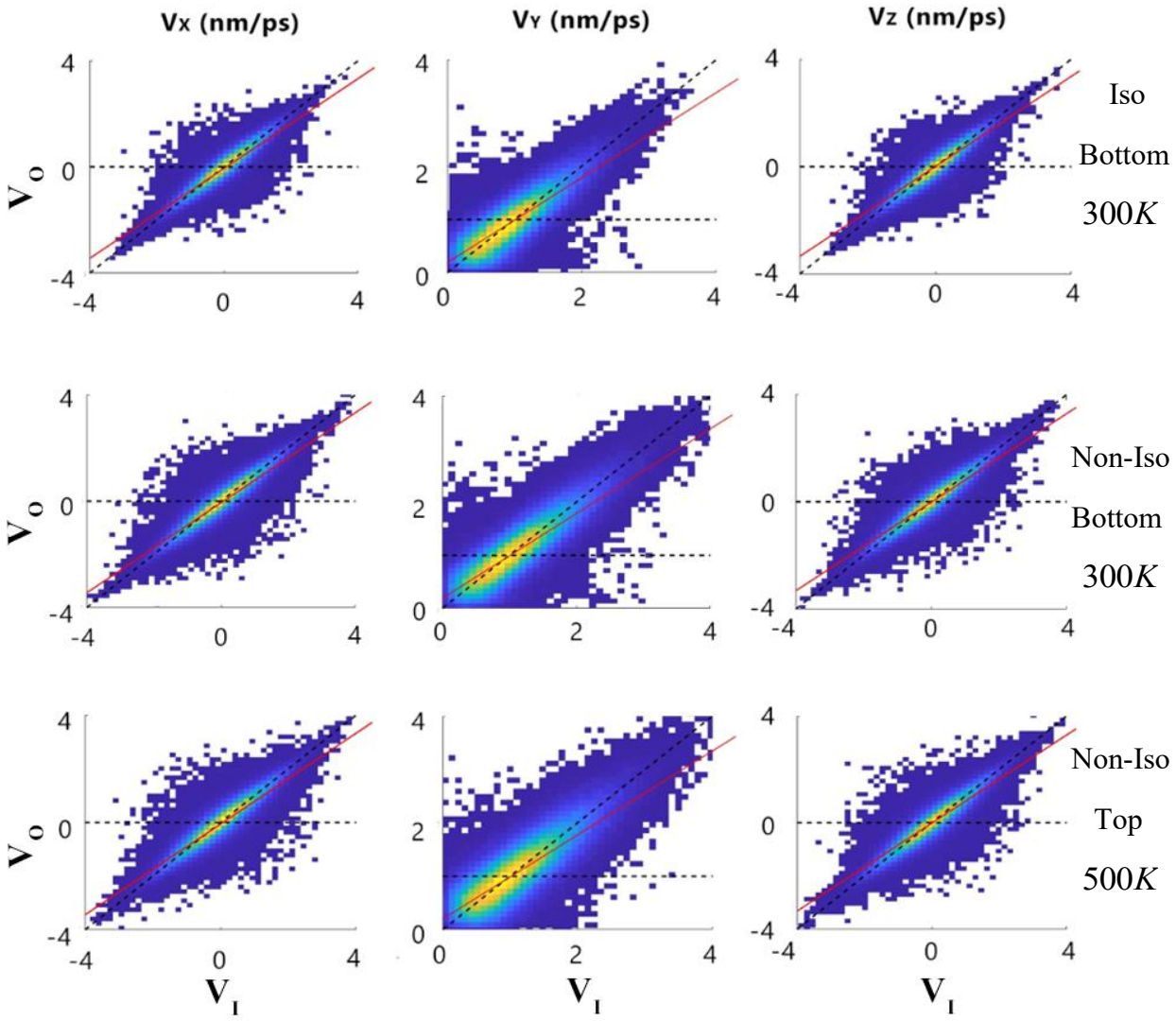

Figure 18: Velocity correlations of x-, y-, z- components of momentum of the He-Au system with surface temperature of T_B=300K/T_T=300K and T_B=300K/T_T=500K.

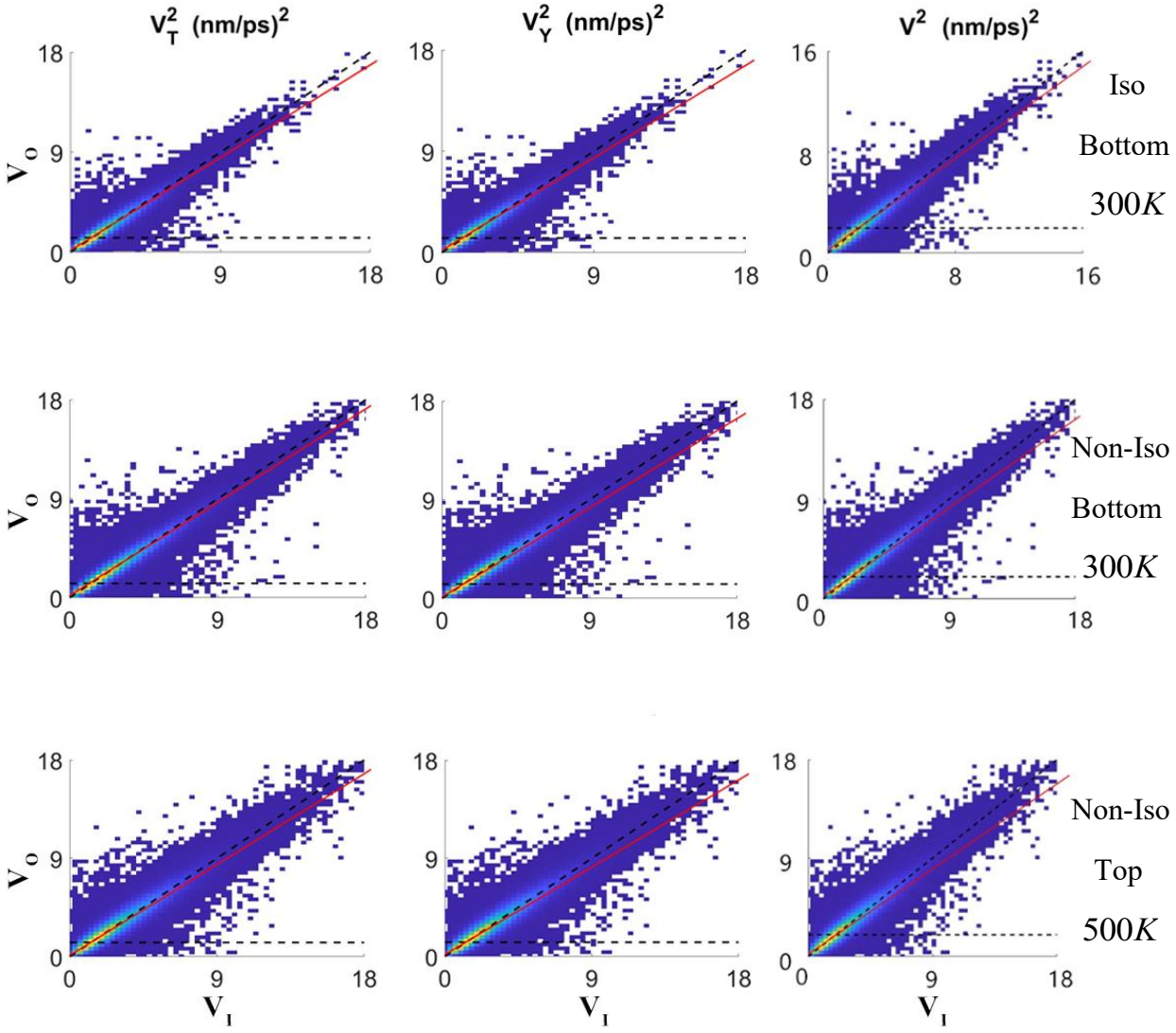

Figure 19: Energy correlations of the He-Au system with surface temperature of T_B=300K/T_T=300K and T_B=300K/T_T=500K.

Table 16: Energy and momentum accommodation coefficients of the Ar-Au system with number densities η=[0.59,0.27,0.18,0.09].

	Ar-Au, η=0.59			Ar-Au, η=0.27		
	[9]	Eq. (4.18)	Eq. (4.1)	[9]	Eq. (4.18)	Eq. (4.1)
a_x	0.824	0.8677	0.76569	-	0.8186	-0.27
a_y	0.913	0.9113	0.75024	-	0.8958	0.7458
a_z	0.832	0.8707	-0.355	-	0.8126	0.036
TMAC	-	0.9147	0.6673	-	0.8792	0.6941
MAC	0.883	0.8773	0.72254	0.846	0.8421	0.7341
a_{vx}^2	-	0.9121	0.60958	-	0.8186	0.6475
a_{vy}^2	-	0.9071	0.7611	-	0.8781	0.7466
a_{vz}^2	-	0.9204	0.76874	-	0.8646	0.7402
EAC	0.874	0.8632	0.72844	0.832	0.8157	0.7227
TEAC	-	0.8967	0.6914	-	0.8527	0.6961

	Ar-Au, η=0.18			Ar-Au, η=0.09		
	[9]	Eq. (4.18)	Eq. (4.1)	[9]	Eq. (4.18)	Eq. (4.1)
a_x	-	0.7900	0.07578	-	0.7461	-0.3864
a_y	-	0.8830	0.8369	-	0.8776	0.8277
a_z	-	0.7985	0.1056	-	0.7469	-0.5783
TMAC	-	0.8536	0.7133	-	0.8146	0.6858
MAC	0.822	0.8153	0.7645	0.791	0.785	0.7761
a_{vx}^2	-	0.8423	0.7005	-	0.8051	0.6858
a_{vy}^2	-	0.8657	0.8496	-	0.8519	0.8356
a_{vz}^2	-	0.8496	0.7202	-	0.8074	0.6643
EAC	0.816	0.7897	0.7614	0.783	0.7522	0.7671
TEAC	-	0.8238	0.7147	-	0.7805	0.6752

Table 17: Energy and momentum accommodation coefficients of the He-Au system with number densities η=[0.048,0.029,0.019,0.009].

	He-Au, η=0.048			He-Au, η=0.029		
	[9]	Eq. (4.18)	Eq. (4.1)	[9]	Eq. (4.18)	Eq. (4.1)
a_x	0.036	0.076	0.082	-	0.0701	-0.0758
a_y	0.113	0.1505	0.0444	-	0.1445	0.0737
a_z	0.038	0.0746	-0.33	-	0.0687	0.0715
TMAC	-	0.1213	0.0403	-	0.1193	0.0299
MAC	0.059	0.0582	0.0477	0.057	0.0525	0.0481
a_{vx}^2	-	0.1112	0.0294	-	0.1087	0.0503
a_{vy}^2	-	0.1296	0.0566	-	0.1251	0.0632
a_{vz}^2	-	0.1198	0.006	-	0.1106	0.0217
EAC	0.048	0.0475	0.0342	0.046	0.0444	0.0462
TEAC	-	0.0967	0.0171	-	0.0934	0.0346

	He-Au, η=0.019			He-Au, η=0.009		
	[9]	Eq. (4.18)	Eq. (4.1)	[9]	Eq. (4.18)	Eq. (4.1)
a_x	-	0.0625	-0.0346	-	0.0612	0.0599
a_y	-	0.1404	0.0549	-	0.1369	0.0751
a_z	-	0.0631	5.6363	-	0.0572	-9.0634
TMAC	-	0.1116	0.0226	-	0.1081	0.0286
MAC	0.052	0.0455	0,0401	0.049	0.0442	0.0494
a_{vx}^2	-	0.1016	0.0301	-	0.1031	0.0741
a_{vy}^2	-	0.1218	0.0039	-	0.1219	0.0651
a_{vz}^2	-	0.1065	0.0248	-	0.0951	-0.0089
EAC	0.043	0.0378	0.0031	0.042	0.0367	0.0477
TEAC	-	0.0893	0.0023	-	0.0837	0.0344

Table 18: Energy and momentum accommodation coefficients of the Ar-Au system with surface temperature of T_B=300K/T_T=300K and T_B=300K/T_T=500K.

	Ar-Au Isothermal			*Ar-Au Non-Iso*					
	Bottom Wall 300 K			*Bottom Wall 300 K*			*Top Wall 500 K*		
	[25]	Eq. (4.18)	Eq. (4.1)	[25]	Eq. (4.18)	Eq. (4.1)	[25]	Eq. (4.18)	Eq. (4.1)
a_x	0.876	0.8692	-4.333	0.886	0.8691	0.5731	0.775	0.7637	-0.8431
a_y	-	0.9123	0.304	-	0.90467	0.7155	-	0.8568	0.6457
a_z	0.888	0.8795	0.055	0.884	0.8735	0.278	0.777	0.7644	-0.4559
TMAC	-	0.9205	0.2943	-	0.9095	0.6374	-	0.8491	0.5036
MAC	-	0.8861	0.333	-	0.8742	0.6795	-	0.8121	0.5782
a_{vx}^2	-	0.9113	0.1972	-	0.9154	0.622	-	0.8410	0.451
a_{vy}^2	0.91	0.9078	0.7862	0.91	0.9038	0.745	0.856	0.8422	0.6497
a_{vz}^2	-	0.9255	0.4206	-	0.9205	0.6453	-	0.7796	0.4751
EAC	0.873	0.8714	0.4285	0.873	0.8681	0.6937	0.792	0.7796	0.5612
TEAC	-	0.9010	0.3625	-	0.8992	0.6341	-	0.8183	0.4630

Table 19: Energy and momentum accommodation coefficients of the He-Au system with surface temperature of T_B=300K/T_T=300K and T_B=300K/T_T=500K.

	He-Au Isothermal Bottom Wall 300 K			He-Au Non-Iso Bottom Wall 300 K			Top Wall 500 K		
	[25]	Eq. (4.18)	Eq. (4.1)	[25]	Eq. (4.18)	Eq. (4.1)	[25]	Eq. (4.18)	Eq. (4.1)
a_x	0.073	0.0727	0.0242	0.072	0.0716	0.0501	0.079	0.0788	-9.8305
a_y	-	0.1555	-0.0084	-	0.1342	0.0466	-	0.1691	0.0557
a_z	0.073	0.0729	0.2843	0.07	0.0697	-2.2915	0.083	0.0791	-0.0369
TMAC	-	0.1237	-0.0235	-	0.1191	0.0101	-	0.1347	0.0136
MAC	-	0.0599	0.0499	-	0.0481	0.0295	-	0.0612	0.0337
a_{vx}^2	-	0.1160	-0.1414	-	0.1159	0.0171	-	0.1258	0.0156
a_{vy}^2	0.132	0.1283	0.1043	0.126	0.1249	0.0488	0.137	0.1432	0.0457
a_{vz}^2	-	0.1168	-0.0057	-	0.1095	0.0083	-	0.1216	0.0097
EAC	0.05	0.0474	0.1142	0.045	0.0431	0.0305	0.046	0.0473	0.0297
TEAC	-	0.0986	-0.0641	-	0.0961	0.0126	-	0.1069	0.0126

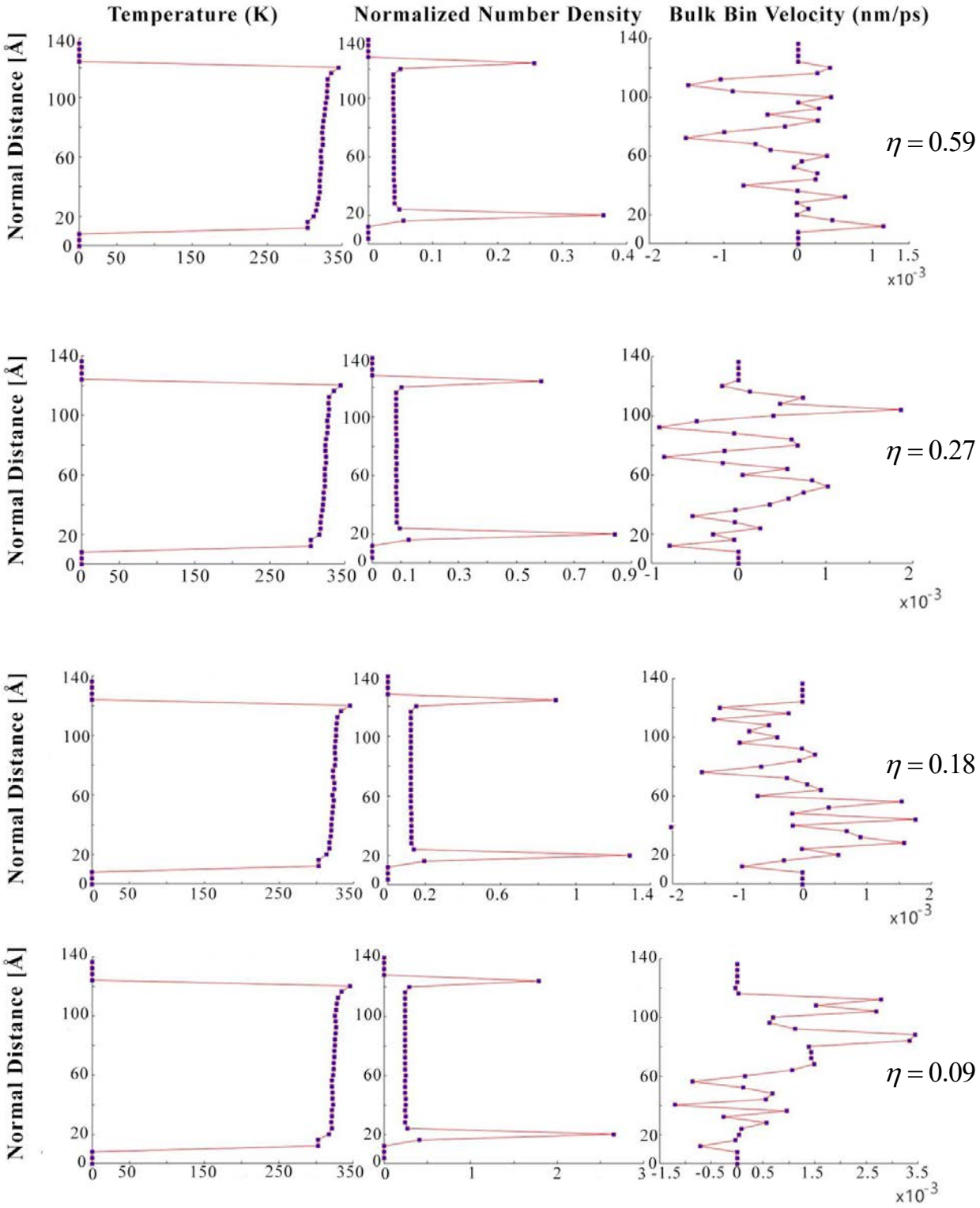

Figure 20: Macroscopic quantities of the Ar-Au system with number densities η=[0.59,0.27,0.18,0.09].

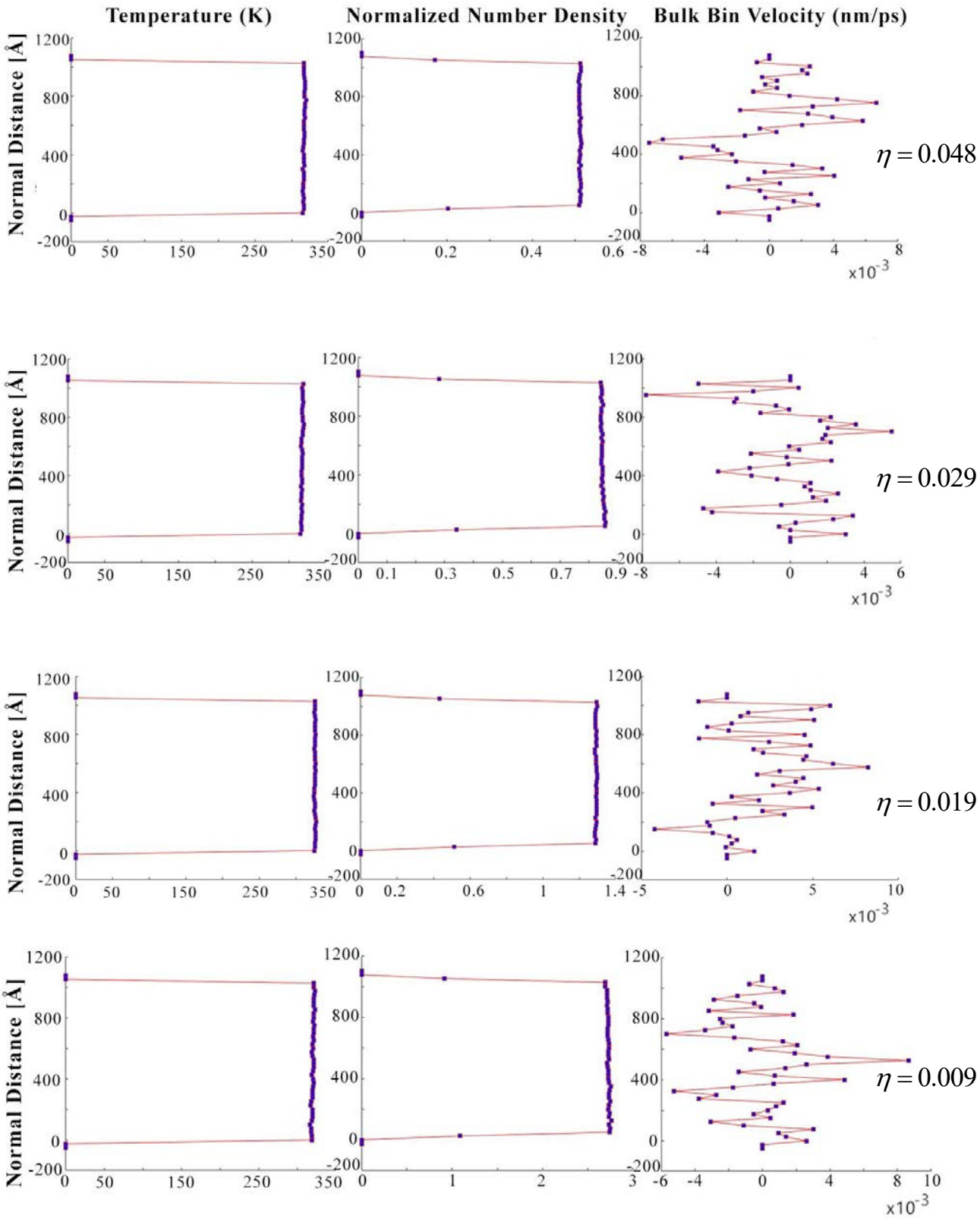

Figure 21: Macroscopic quantities of the He-Au system with number densities η=[0.048,0.029,0.019,0.009].

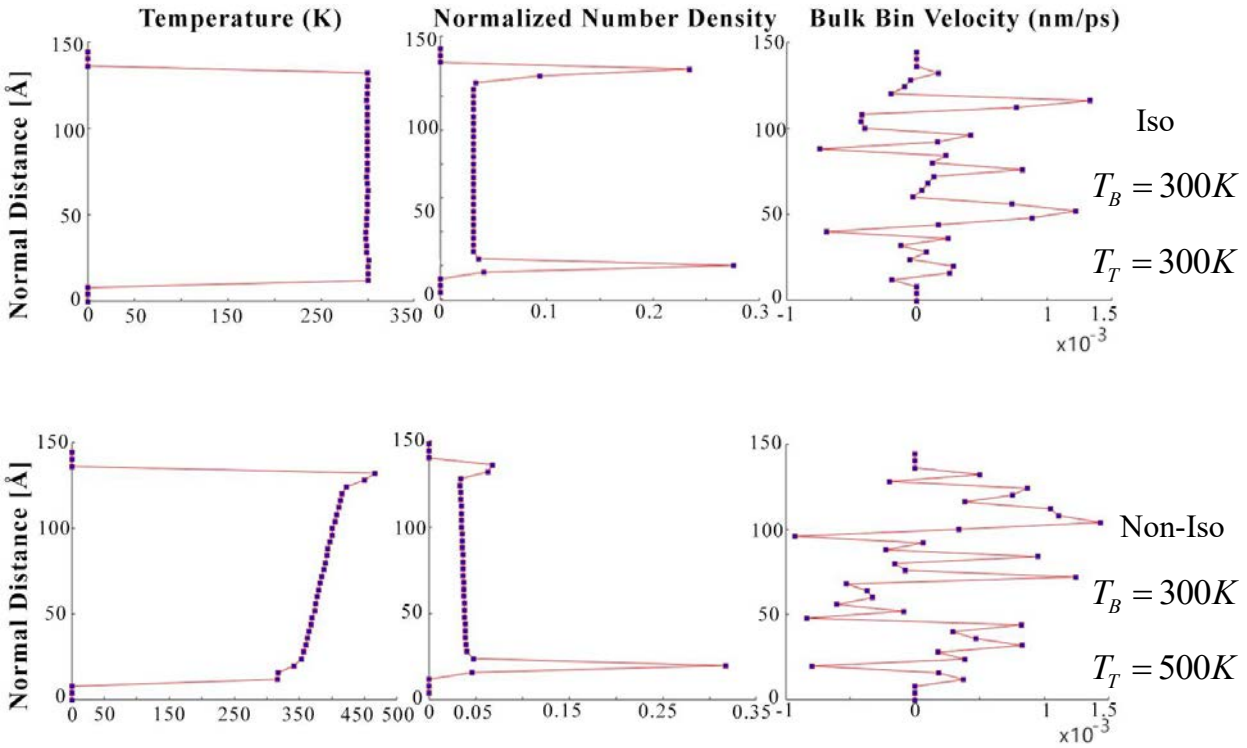

Figure 22: Macroscopic quantities of the Ar-Au system with surface temperature of T_B=300K/T_T=300K and T_B=300K/T_T=500K.

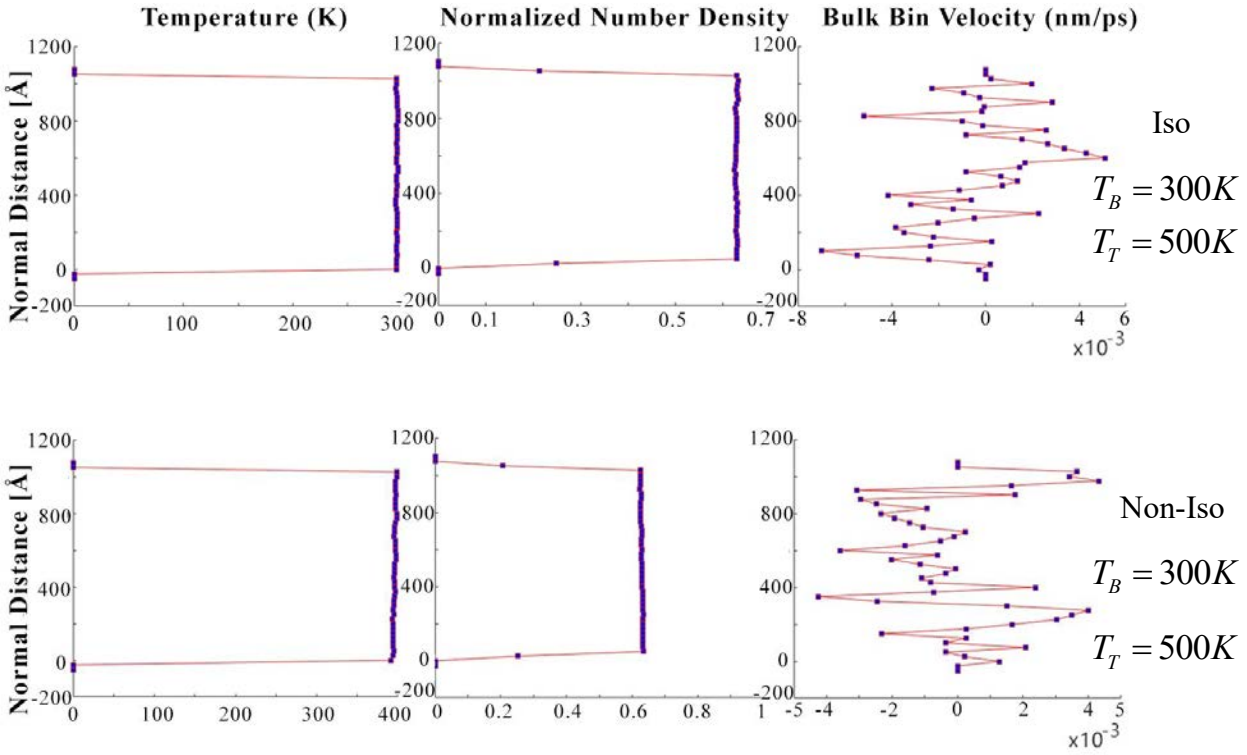

Figure 23: Indicative macroscopic quantities of the He-Au system with surface temperature of T_B=300K/T_T=300K and T_B=300K/T_T=500K.

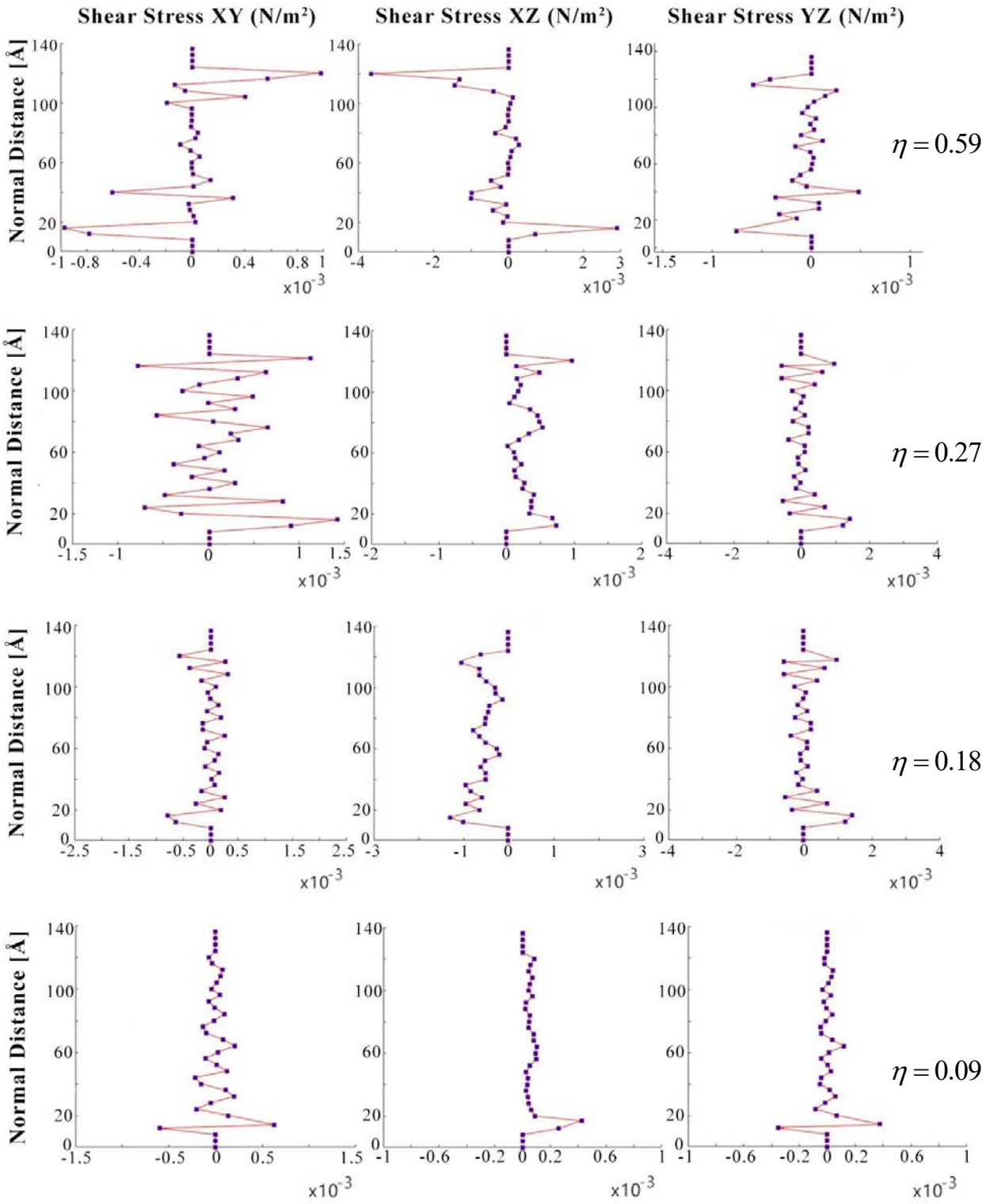

Figure 24: Shear stress of the Ar-Au system with number densities η=[0.59,0.27,0.18,0.09].

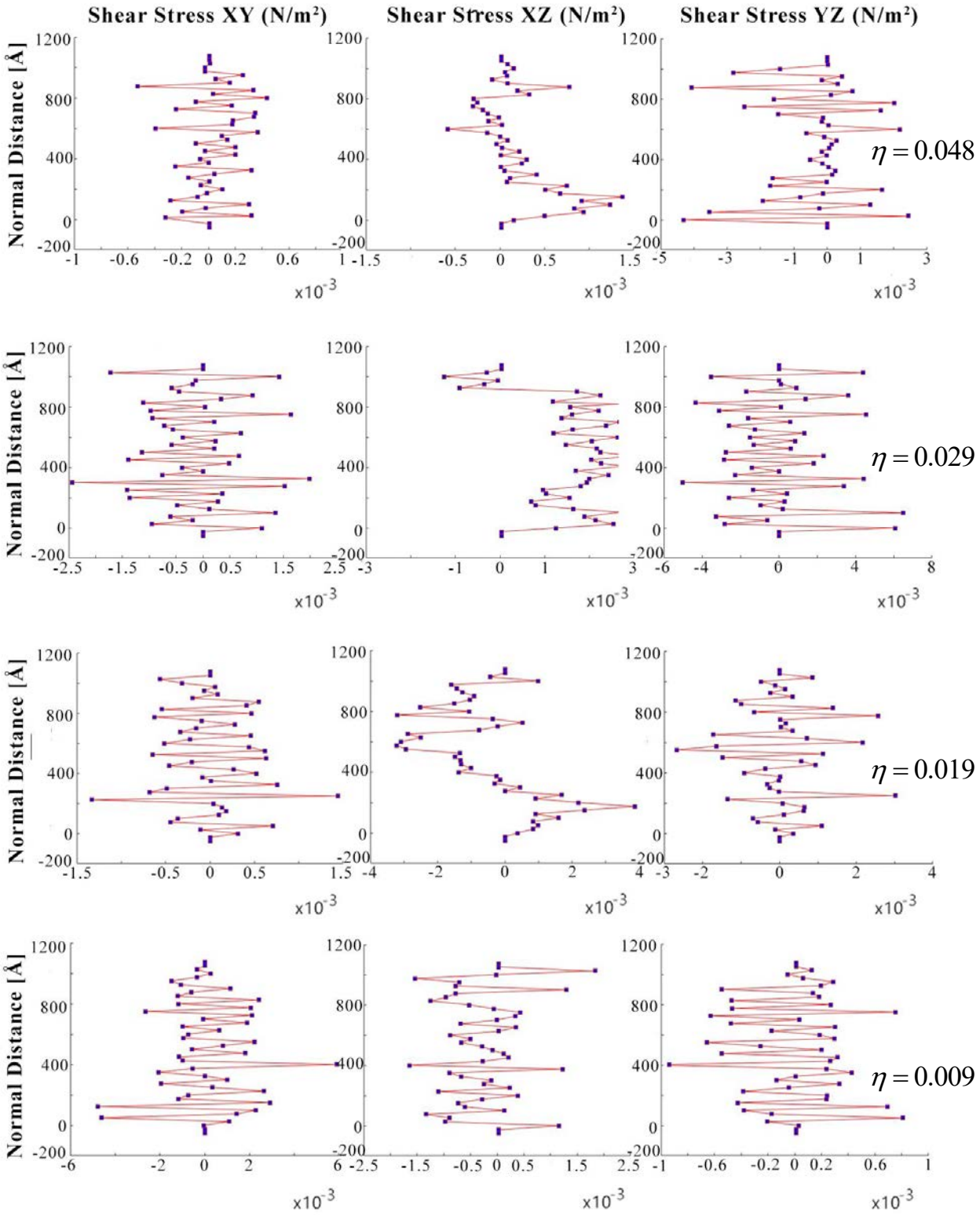

Figure 25: Shear stress of the He-Au system with number densities η=[0.048,0.029,0.019,0.009].

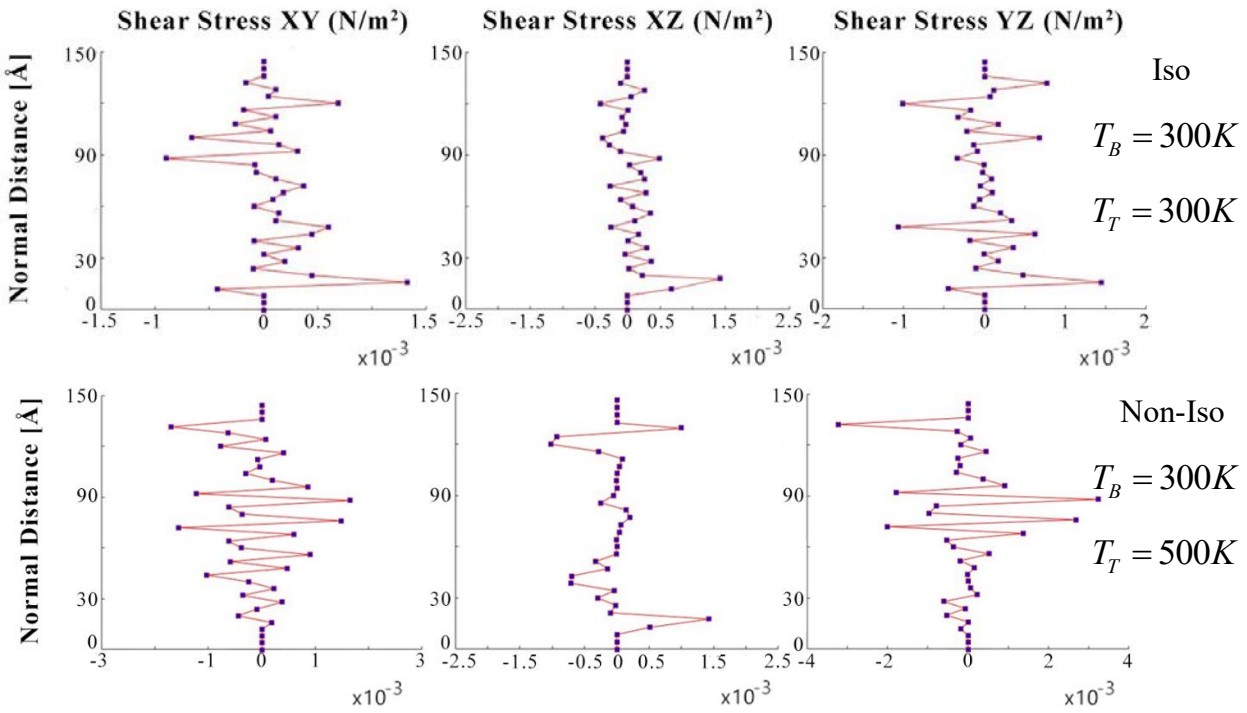

Figure 26: Shear stress of the Ar-Au system for surface temperatures of T_B=300K/T_T=300K and T_B=300K/T_T=500K.

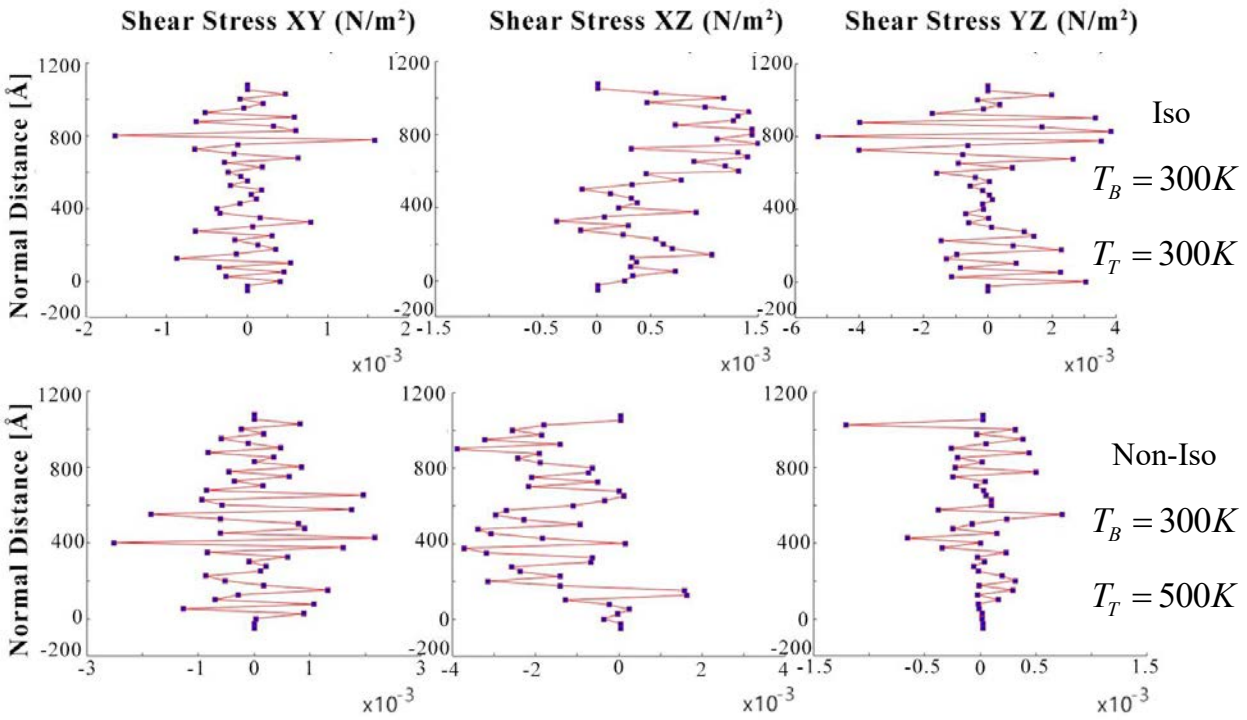

Figure 27: Shear stress of the He-Au system for surface temperatures of T_B=300K/T_T=300K and T_B=300K/T_T=500K.

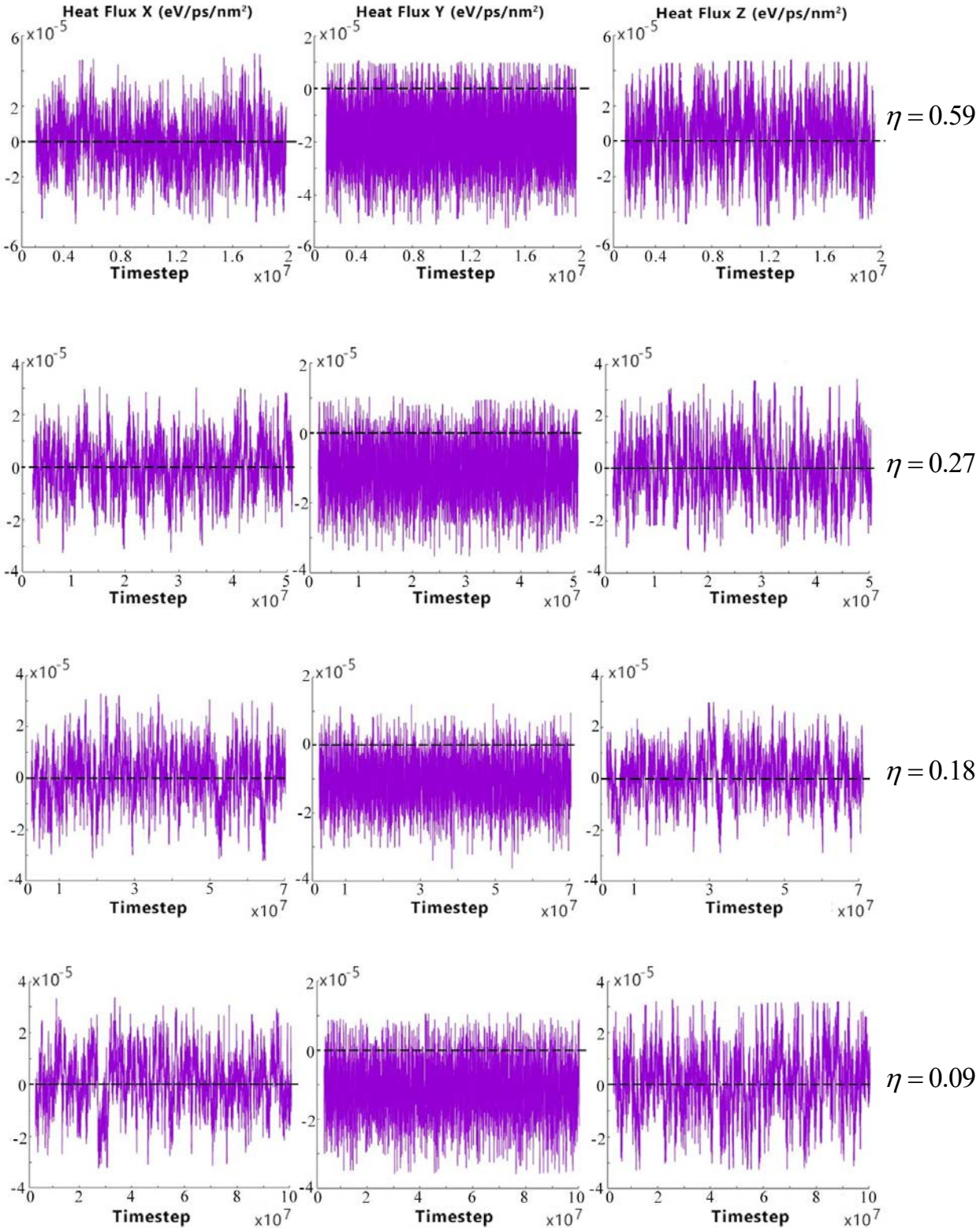

Figure 28: Heat flux of the Ar-Au system with number densities η=[0.59,0.27,0.18,0.09].

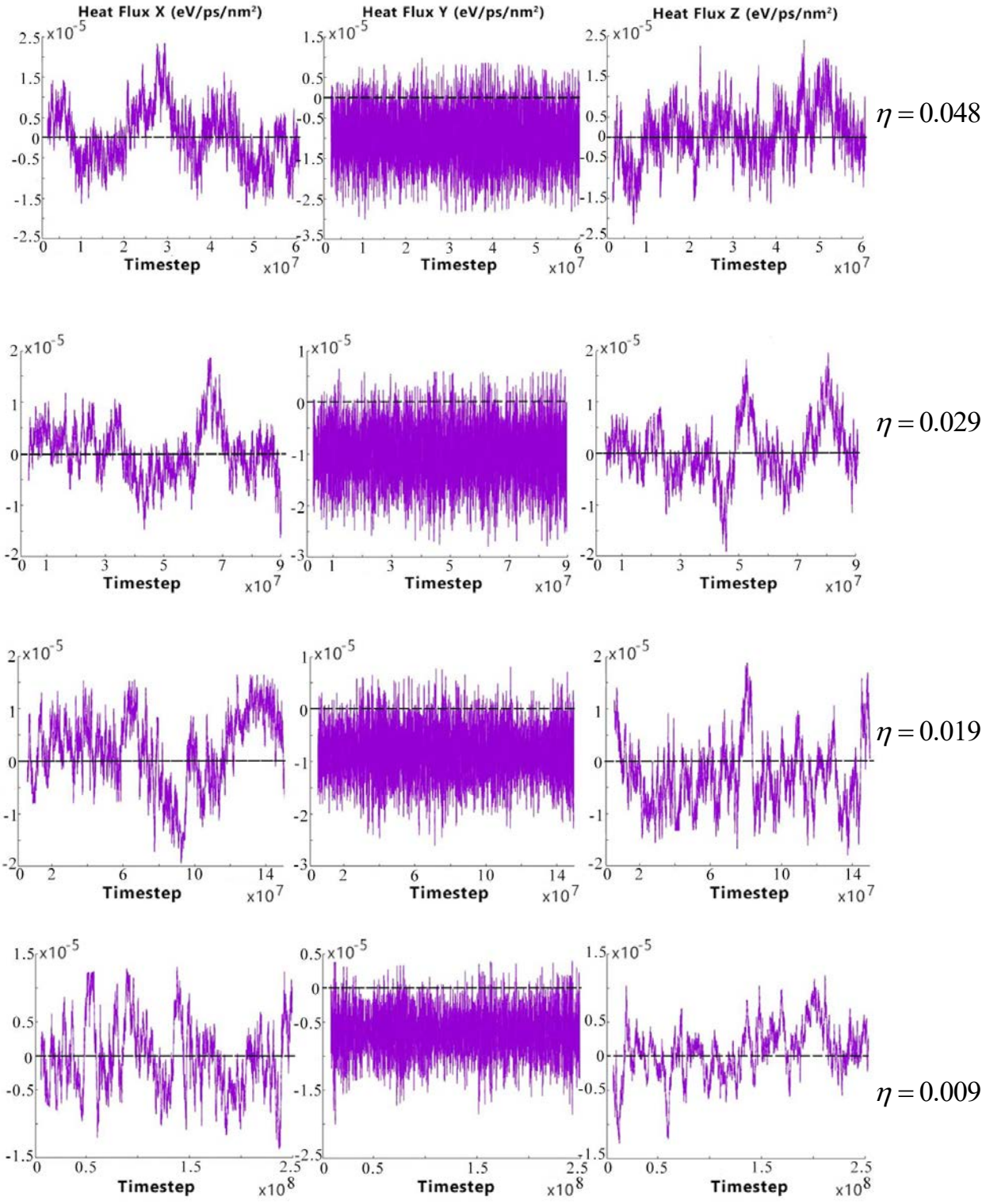

Figure 29: Heat flux of the He-Au system with number densities η=[0.048,0.029,0.019,0.009].

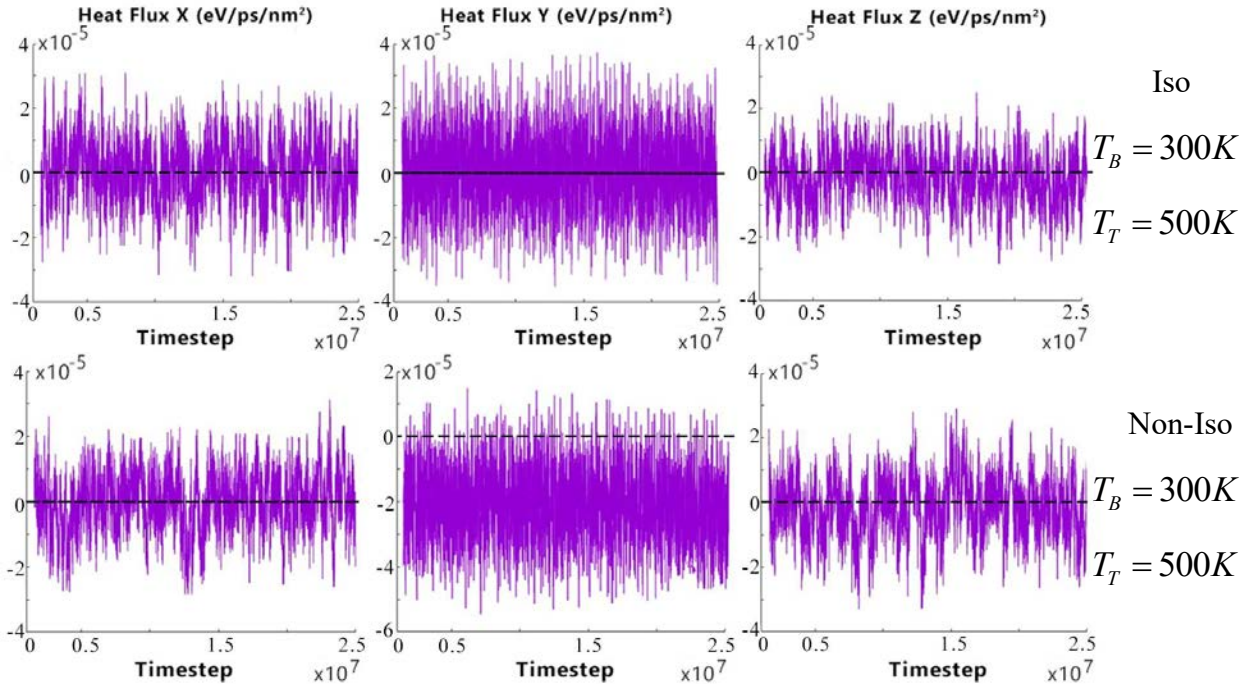

Figure 30: Heat flux of the Ar-Au system for surface temperatures of T_B=300K/T_T=300K and T_B=300K/T_T=500K.

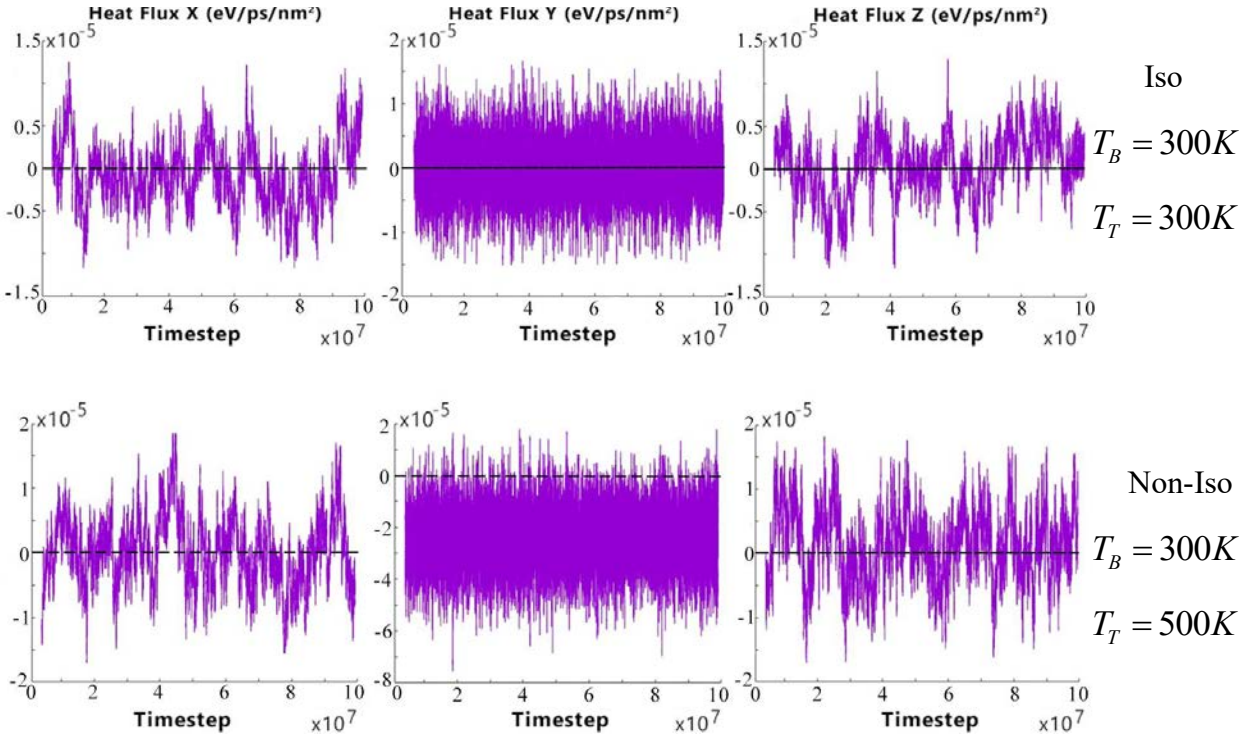

Figure 31: Heat flux of the He-Au system for surface temperatures of T_B=300K/T_T=300K and T_B=300K/T_T=500K.

Chapter 6: **CONCLUDING REMARKS AND FUTURE WORK**

In this study, the gas-surface interactions in the heat transfer, between Argon and Helium and two parallel gold walls, were investigated using MD simulations. In the first scenario of applying various number densities, the effects of gas pressure on the E/MACs, velocity correlation shapes, and velocity distributions were studied for both Ar-Au and He-Au systems. By comparing the results of the densest and least dense case for both systems, it was shown that a decrease in the gas pressure resulted in an average decrease of 11% and 16% in every E/MAC except for the normal E/MAC which exhibited an average decrease of 5% and 7% in the Ar-Au and He-Au systems respectively. In addition, a change towards the specular model was observed in the shape and velocity distribution of the tangential components in both systems. In the second scenario of applying various temperature gradients, the effects of different surface temperatures on the E/MACs, velocity correlation shapes, and velocity distributions were investigated for both Ar-Au and He-Au systems. Increasing the surface temperature gradient resulted in an average decrease of 9% in the Ar-Au system and an average increase of 14% in the He-Au system in every E/MAC. In addition, the shape and the velocity distribution of every velocity correlation of the Ar-Au system aligned more closely with the specular model, in comparison with the He-Au system where no significant changes were observed. All E/MAC values were compared with those of similar case studies that applied a different EAM potential to the walls. The results showed a strong correlation, indicating that the findings were consistent with [9],[25]. The macroscopic quantities that emerged from the particle interactions were analyzed to ensure the accuracy and reliability of the results by comparing them with the theory of the Fourier flow. In addition, the computational effort for each case was studied. While reducing the gas pressure increased the time required for the MD simulation due to fewer collisions, increasing the temperature gradient did not affect the simulation time.

For future work, a promising case study could be the investigation of the E/MACs and macroscopic quantities of the tungsten-helium system. This system is particularly relevant in the context of nuclear reactors, where helium is used as a coolant and interacts with tungsten-made reactor components. Understanding these interactions at both the microscopic and macroscopic levels could provide valuable insights into the performance, safety, and efficiency of the reactor system.

REFERENCES

[1] C. Shen, *Rarefied Gas Dynamics*. in Heat and Mass Transfer. Berlin, Heidelberg: Springer Berlin Heidelberg, 2005. doi: 10.1007/B138784.

[2] H. Sha, R. Faller, G. Tetiker, and P. Woytowitz, "Molecular simulation study of aluminum–noble gas interfacial thermal accommodation coefficients," *AIChE Journal*, vol. 64, no. 1, pp. 338–345, Jan. 2018, doi: 10.1002/AIC.15886.

[3] L. Wu, *Rarefied Gas Dynamics: Kinetic Modeling and Multi-Scale Simulation*. Springer Nature, 2022. doi: 10.1007/978-981-19-2872-7/COVER.

[4] J. Sun and Z. X. Li, "Molecular dynamics simulations of energy accommodation coefficients for gas flows in nano-channels," *Mol Simul*, vol. 35, no. 3, pp. 228–233, Mar. 2009, doi: 10.1080/08927020802395435.

[5] P. Spijker, A. J. Markvoort, S. V. Nedea, and P. A. J. Hilbers, "Computation of accommodation coefficients and the use of velocity correlation profiles in molecular dynamics simulations," *Phys Rev E Stat Nonlin Soft Matter Phys*, vol. 81, no. 1, p. 011203, Jan. 2010, doi: 10.1103/PHYSREVE.81.011203/FIGURES/7/MEDIUM.

[6] S. K. Prabha and S. P. Sathian, "Determination of accommodation coefficients of a gas mixture in a nanochannel with molecular dynamics," *Microfluid Nanofluidics*, vol. 13, no. 6, pp. 883–890, Dec. 2012, doi: 10.1007/S10404-012-1020-9/METRICS.

[7] J. Sun and Z. X. Li, "Three-Dimensional Molecular Dynamic Study on Accommodation Coefficients in Rough Nanochannels," *Heat Transfer Engineering*, vol. 32, no. 7–8, pp. 658–666, Jun. 2011, doi: 10.1080/01457632.2010.509759.

[8] S. V. Nedea, A. A. Van Steenhoven, A. J. Markvoort, P. Spijker, and D. Giordano, "Gas-surface interactions using accommodation coefficients for a dilute and a dense gas in a micro- or nanochannel: Heat flux predictions using combined molecular dynamics and Monte Carlo techniques," *Phys Rev E Stat Nonlin Soft Matter Phys*, vol. 89, no. 5, p. 053012, May 2014, doi: 10.1103/PHYSREVE.89.053012/FIGURES/10/MEDIUM.

[9] S. M. Nejad, S. Nedea, A. Frijns, and D. Smeulders, "The Influence of Gas–Wall and Gas–Gas Interactions on the Accommodation Coefficients for Rarefied Gases: A Molecular Dynamics Study," *Micromachines 2020, Vol. 11, Page 319*, vol. 11, no. 3, p. 319, Mar. 2020, doi: 10.3390/MI11030319.

[10] B. Y. Cao, J. Sun, M. Chen, and Z. Y. Guo, "Molecular Momentum Transport at Fluid-Solid Interfaces in MEMS/NEMS: A Review," *International Journal of Molecular Sciences 2009, Vol. 10, Pages 4638-4706*, vol. 10, no. 11, pp. 4638–4706, Oct. 2009, doi: 10.3390/IJMS10114638.

[11] H. Kamberaj, *Molecular Dynamics Simulations in Statistical Physics: Theory and Applications*. in Scientific Computation. Cham: Springer International Publishing, 2020. doi: 10.1007/978-3-030-35702-3.

[12] D. Frenkel and B. Smit, "Understanding Molecular Simulation: Monte Carlo Simulations in Various Ensembles," *Academic Press, London*, pp. 111–137, 2002, Accessed: Apr. 07, 2024. [Online]. Available: https://www.sciencedirect.com/science/article/pii/B9780122673511500079

[13] D. C. Rapaport, *The Art of Molecular Dynamics Simulation*. Cambridge University Press, 2004. doi: 10.1017/CBO9780511816581.

[14] S. Mubin, J. Li, and S. Plimpton, *Extending and Modifying LAMMPS Writing Your Own Source Code*. Packt Publishing Ltd, 2021.

[15] K. Zhou and B. Liu, *Molecular Dynamics Simulation: Fundamentals and Applications*. Elsevier, 2022. doi: 10.1016/B978-0-12-816419-8.00001-5.

[16] S. Li and J. Li, *Introduction to Computational Nanomechanics Multiscale and Statistical Simulations*. 2022.

[17] M. S. Daw, S. M. Foiles, and M. I. Baskes, "The embedded-atom method: a review of theory and applications," *Materials Science Reports*, vol. 9, no. 7–8, pp. 251–310, Mar. 1993, doi: 10.1016/0920-2307(93)90001-U.

[18] A. Agrawal, "A Comprehensive Review on Gas Flow in Microchannels," *Int J Micronano Scale Transp*, vol. 2, no. 1, pp. 1–40, Mar. 2011, doi: 10.1260/1759-3093.2.1.1.

[19] J. E. Basconi and M. R. Shirts, "Effects of temperature control algorithms on transport properties and kinetics in molecular dynamics simulations," *J Chem Theory Comput*, vol. 9, no. 7, pp. 2887–2899, Jul. 2013, doi: 10.1021/CT400109A.

[20] A. P. Thompson *et al.*, "LAMMPS - a flexible simulation tool for particle-based materials modeling at the atomic, meso, and continuum scales," *Comput Phys Commun*, vol. 271, p. 108171, Feb. 2022, doi: 10.1016/J.CPC.2021.108171.

[21] S. M. Foiles, M. I. Baskes, and M. S. Daw, "Embedded-atom-method functions for the fcc metals Cu, Ag, Au, Ni, Pd, Pt, and their alloys," *Phys Rev B*, vol. 33, no. 12, pp. 7983–7991, 1986, doi: 10.1103/PHYSREVB.33.7983.

[22] R. Grenier, Q. D. To, M. P. De Lara-Castells, and C. Léonard, "Argon Interaction with Gold Surfaces: Ab Initio-Assisted Determination of Pair Ar-Au Potentials for Molecular Dynamics Simulations," *Journal of Physical Chemistry A*, vol. 119, no. 26, pp. 6897–6908, Jul. 2015, doi: 10.1021/ACS.JPCA.5B03769/SUPPL_FILE/JP5B03769_SI_001.PDF.

[23] M. Liao, R. Grenier, Q. D. To, M. P. De Lara-Castells, and C. Léonard, "Helium and Argon Interactions with Gold Surfaces: Ab Initio-Assisted Determination of the He-Au Pairwise

Potential and Its Application to Accommodation Coefficient Determination," *Journal of Physical Chemistry C*, vol. 122, no. 26, pp. 14606–14614, Jul. 2018, doi: 10.1021/ACS.JPCC.8B03555/ASSET/IMAGES/LARGE/JP-2018-03555M_0004.JPEG.

[24] S. K. Prabha and S. P. Sathian, "Computational study of thermal dependence of accommodation coefficients in a nano-channel and the prediction of velocity profiles," *Comput Fluids*, vol. 68, pp. 47–53, Sep. 2012, doi: 10.1016/J.COMPFLUID.2012.07.021.

[25] S. Mohammad Nejad, E. Iype, S. Nedea, A. Frijns, and D. Smeulders, "Modeling rarefied gas-solid surface interactions for Couette flow with different wall temperatures using an unsupervised machine learning technique," *Phys Rev E*, vol. 104, no. 1, p. 015309, Jul. 2021, doi: 10.1103/PHYSREVE.104.015309/FIGURES/25/MEDIUM.

[26] H. W. Sheng, M. J. Kramer, A. Cadien, T. Fujita, and M. W. Chen, "Highly optimized embedded-atom-method potentials for fourteen FCC metals," *Phys Rev B Condens Matter Mater Phys*, vol. 83, no. 13, p. 134118, Apr. 2011, doi: 10.1103/PHYSREVB.83.134118/FIGURES/14/MEDIUM.

[27] B. Y. Cao, M. Chen, and Z. Y. Guo, "Temperature dependence of the tangential momentum accommodation coefficient for gases," *Appl Phys Lett*, vol. 86, no. 9, pp. 1–3, Feb. 2005, doi: 10.1063/1.1871363/328777.

APPENDIX

The equilibrium LAMMPS code and the production LAMMPS code of the Ar-Au setup, with a number density η=0.59 are provided.

A.1 Equilibrium LAMMPS code

At the start of the equilibrium code, the dimensions of the region, boundary conditions, neighbor-list skin width, units, atom style, and lattice are defined. In the second step, the sub-regions and groups are defined along with the atom masses and potential parameters. The Au walls and the gases are placed in the region and an energy minimization is applied. When the system reaches the minimum energy state, the initial speed of the gas particles is defined by applying Eq. (2.15) by defining the initial temperature. Finally, the Berendsen thermostats and spring potentials are defined along with some variables to check the system properties. In addition, a restart file and the position data of each particle are exported.

```
dimension 3

units metal

boundary p p p

atom_style atomic

neighbor 2.5 bin

neigh_modify delay 0 every 1 check yes

lattice fcc 4.08


#region

region box block 0 100 -11.5 151.5 0 100 units box

create_box 2 box


region BottomWall block INF INF 0 12.5 INF INF units box

region Arreg block INF INF 14 124 INF  INF units box

region TopWall block INF INF 125.5 140 INF INF units box

region BotVac block INF INF -11.5 -1.5 INF INF units box

region TopVac block INF INF 141.5 151.5 INF INF   units box


#FixLayers
```

```
region BottomwallFix block INF INF -1.45 1.7857 INF INF units box
region TopwallFix block INF INF 137.2 140.4 INF INF units box



#mass
mass 1 196.96 #Au
mass 2 39.94 #Ar

#Au walls
create_atoms 1 region BottomWall
create_atoms 1 region TopWall

group TopWall region TopWall
group BottomWall region BottomWall
group BottomwallFix region BottomwallFix
group TopwallFix region TopwallFix
group TopVac region TopVac
group BotVac region BotVac

#Potentials
pair_style hybrid eam lj/cut 8.375
pair_coeff 1 1 eam Au_u3.eam
pair_coeff 2 2 lj/cut 0.0122 3.35 8.375
pair_coeff 1 2 lj/cut 0.01136 3.819 12

timestep    0.001
# Placement of Ar
region      ArMiddle block 0 100 53 85 0 100 units box
```

```
group       Ar type 2


fix         placeAr Ar deposit 649 2 5 12345 region ArMiddle near 4 units box
variable    CountAr equal count(Ar)
thermo_style    custom step atoms temp epair etotal press v_CountAr
thermo      50
run         3245
unfix       placeAr


#Energy Minimization
min_style cg
minimize 1e-16 1e-16 100000 100000


#Initial Temperature
velocity Ar create 300 123456 mom yes rot yes dist uniform


reset_timestep 0


#------------------------------------------------------------------------
compute     TWBtot BottomWall temp
compute     TWBcom BottomWall temp/com
compute     TWBx BottomWall temp/partial 1 0 0
compute     TWBy BottomWall temp/partial 0 1 0
compute     TWBz BottomWall temp/partial 0 0 1
compute     TWByz BottomWall temp/partial 0 1 1
#------------------------------------------------------------------------
compute     TWTtot TopWall temp
compute     TWTcom TopWall temp/com
```

```
compute     TWTx TopWall temp/partial 1 0 0
compute     TWTy TopWall temp/partial 0 1 0
compute     TWTz TopWall temp/partial 0 0 1
compute     TWTyz TopWall temp/partial 0 1 1
#-------------------------------------------------------------------------
compute     TAr Ar temp
compute     TArCOM Ar temp/com
#-------------------------------------------------------------------------


#-------------------------------------------------------------------------
compute     CGWB BottomwallFix com
compute         CGWT TopwallFix com
#-------------------------------------------------------------------------
compute     peratom all stress/atom NULL
compute     p all reduce sum c_peratom[1] c_peratom[2] c_peratom[3]
variable        myPress equal -(c_p[1]+c_p[2]+c_p[3])/(3*vol)
#-------------------------------------------------------------------------
compute     peratomAr Ar stress/atom NULL
compute     pAr Ar reduce sum c_peratomAr[1] c_peratomAr[2] c_peratomAr[3]
variable        myPressAr equal -(c_pAr[1]+c_pAr[2]+c_pAr[3])/(3*100*100*110)
#-------------------------------------------------------------------------


timestep 0.001
fix 1 all nve


fix 2 TopWall temp/berendsen 350 350 0.1
fix_modify 2 temp TWTtot
fix 3 BottomWall temp/berendsen 300 300 0.1
fix_modify 3 temp TWBtot
```

```
fix 4 BottomwallFix spring/self 10 y
fix 5 TopwallFix spring/self 10 y


thermo 1000


thermo_style    custom step c_TWBtot c_TWBcom c_TWTtot c_TWTcom c_TAr c_TArCOM
c_CGWB[2] c_CGWT[2] press v_myPress v_myPressAr
thermo_modify   lost warn


dump        1 all custom 1000 dump-nve059.lammpstrj id type x y z


restart         1000000 fourier_ArAuN059.restart


run         1000000
```

A.2 Production LAMMPS code

The restart file of the equilibrated system is inserted at the start of the production code. Potential parameters and important variables for checking the system properties are defined. In addition, the Berendsen thermostats and spring potentials are applied to the Au walls. Finally, the position and velocity data of each particle along with the heat flux of the system are exported.

```
read_restart fourier_ArAuN059.restart.1000000


pair_style hybrid eam lj/cut 8.375  #siiAr=3.35 A
pair_coeff 1 1 eam Au_u3.eam #eam potential gia Au-Au
pair_coeff 2 2 lj/cut 0.0122 3.35 8.375 #Lennard Jones gia Ar-Ar
pair_coeff 1 2 lj/cut 0.01136 3.819 12 #Lennard Jones gia Au-Ar
```

```
compute     TWBtot BottomWall temp
compute     TWBcom BottomWall temp/com
compute     TWBx BottomWall temp/partial 1 0 0
compute     TWBy BottomWall temp/partial 0 1 0
compute     TWBz BottomWall temp/partial 0 0 1
compute     TWByz BottomWall temp/partial 0 1 1
#------------------------------------------------------------------------
compute     TWTtot TopWall temp
compute     TWTcom TopWall temp/com
compute     TWTx TopWall temp/partial 1 0 0
compute     TWTy TopWall temp/partial 0 1 0
compute     TWTz TopWall temp/partial 0 0 1
compute     TWTyz TopWall temp/partial 0 1 1
#------------------------------------------------------------------------
compute     TAr Ar temp
compute     TArCOM Ar temp/com
#------------------------------------------------------------------------


#------------------------------------------------------------------------
compute     CGWB BottomwallFix com
compute         CGWT TopwallFix com
#------------------------------------------------------------------------
compute     peratom all stress/atom NULL
compute     p all reduce sum c_peratom[1] c_peratom[2] c_peratom[3]
variable        myPress equal -(c_p[1]+c_p[2]+c_p[3])/(3*vol)
#------------------------------------------------------------------------
compute     peratomAr Ar stress/atom NULL
compute     pAr Ar reduce sum c_peratomAr[1] c_peratomAr[2] c_peratomAr[3]
```

```
variable        myPressAr equal -(c_pAr[1]+c_pAr[2]+c_pAr[3])/(3*100*100*110)
#------------------------------------------------------------------------
compute Arke Ar ke/atom
compute Arpe Ar pe/atom

compute flux Ar heat/flux Arke Arpe peratomAr
timestep 0.001
group Au type 1
fix 1 all nve



fix 2 TopWall temp/berendsen 350 350 0.1
fix_modify 2 temp TWTtot
fix 3 BottomWall temp/berendsen 300 300 0.1
fix_modify 3 temp TWBtot

fix 4 BottomwallFix spring/self 10 y
fix 5 TopwallFix spring/self 10 y


thermo 1000

thermo_style    custom step c_TWBtot c_TWBcom c_TWTtot c_TWTcom c_TAr c_TArCOM
c_CGWB[2] c_CGWT[2] press v_myPress v_myPressAr c_flux[1] c_flux[2] c_flux[3]

thermo_modify   lost warn

dump 8 all custom 10000 dumpAll059.lammpstrj id type x y z

dump 1 Ar custom 1000 dumpArN059ar.lammpstrj id x y z vx vy vz
```

```
dump_modify 1 header no pbc yes

dump 4 Au custom 1000 dumpArN059au.lammpstrj id x y z vx vy vz

dump_modify 4 header no pbc yes


dump 2 Ar custom 1 ArVelocitiesN059.dat id y vx vy vz

dump_modify 2 header no pbc yes thresh y >= 24.25 thresh y <= 24.75

restart         1000000 fourier_ArAuN059.restart

run 20000000
```